Electronic Supplementary Information

Nanosupercapacitors with Fractal Structures: Searching Designs to Push the Limit

Liyuan Pei[a,b], Peiyuan Zhuang[a,b,c], Yangye Sun[d], Xiang Zhang[e], Haohui Qiao[a,b], Keyu Zhu[a], Pulickel M. Ajayan[e], Mingxin Ye[*a], Jianfeng Shen[*a]

a Institute of special materials and technology, Fudan University, Shanghai, P. R. China

b Department of Materials Science, Fudan University, Shanghai, P. R. China

c Shanghai Huitian New Material Co., Ltd., Shanghai, P. R. China

d Department of Chemistry and Shanghai Key Laboratory of Molecular Catalysis and Innovative Materials, Fudan University, Shanghai, P. R. China

e Department of Materials Science and NanoEngineering, Rice University, Houston, TX, USA

*Corresponding Author. Email: mxye@fudan.edu.cn, jfshen@fudan.edu.cn

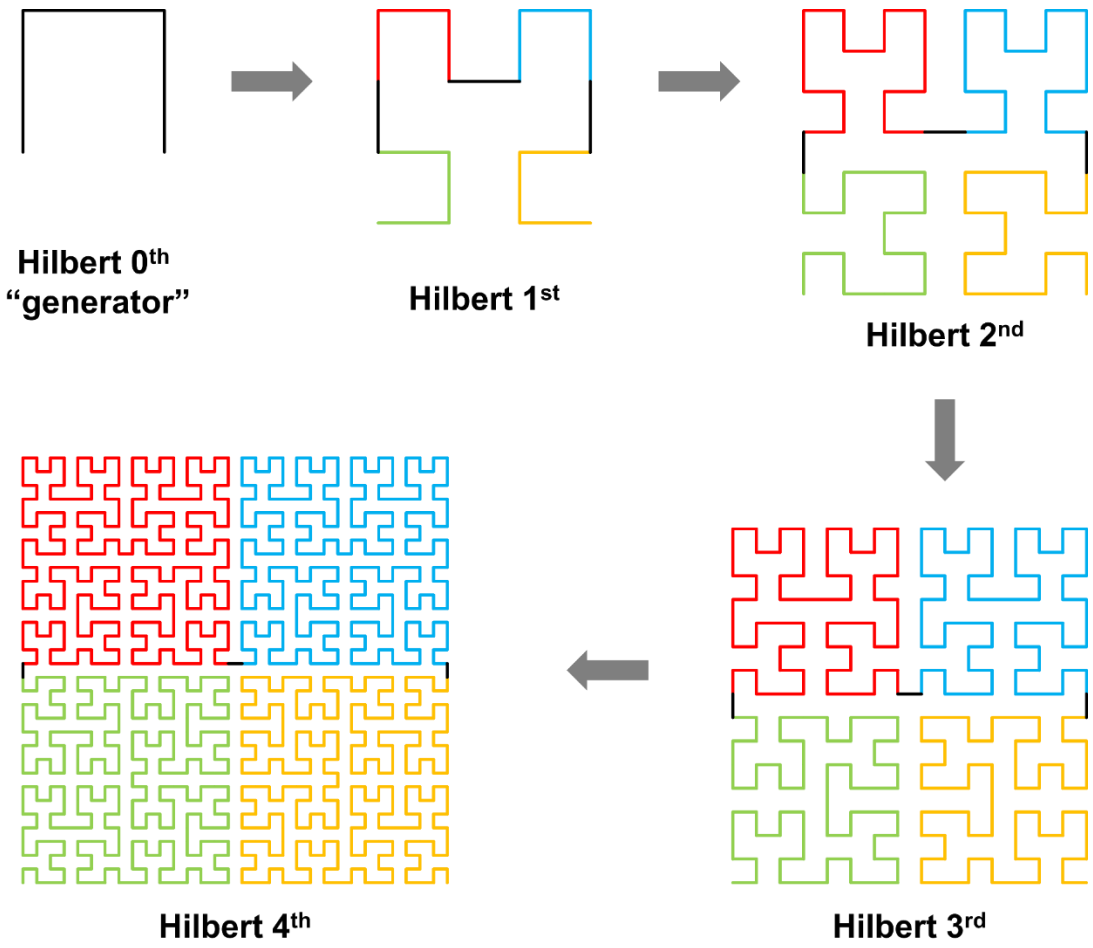

Fig. S1. Construction of Hilbert curves from a "generator" to its 4th iteration.

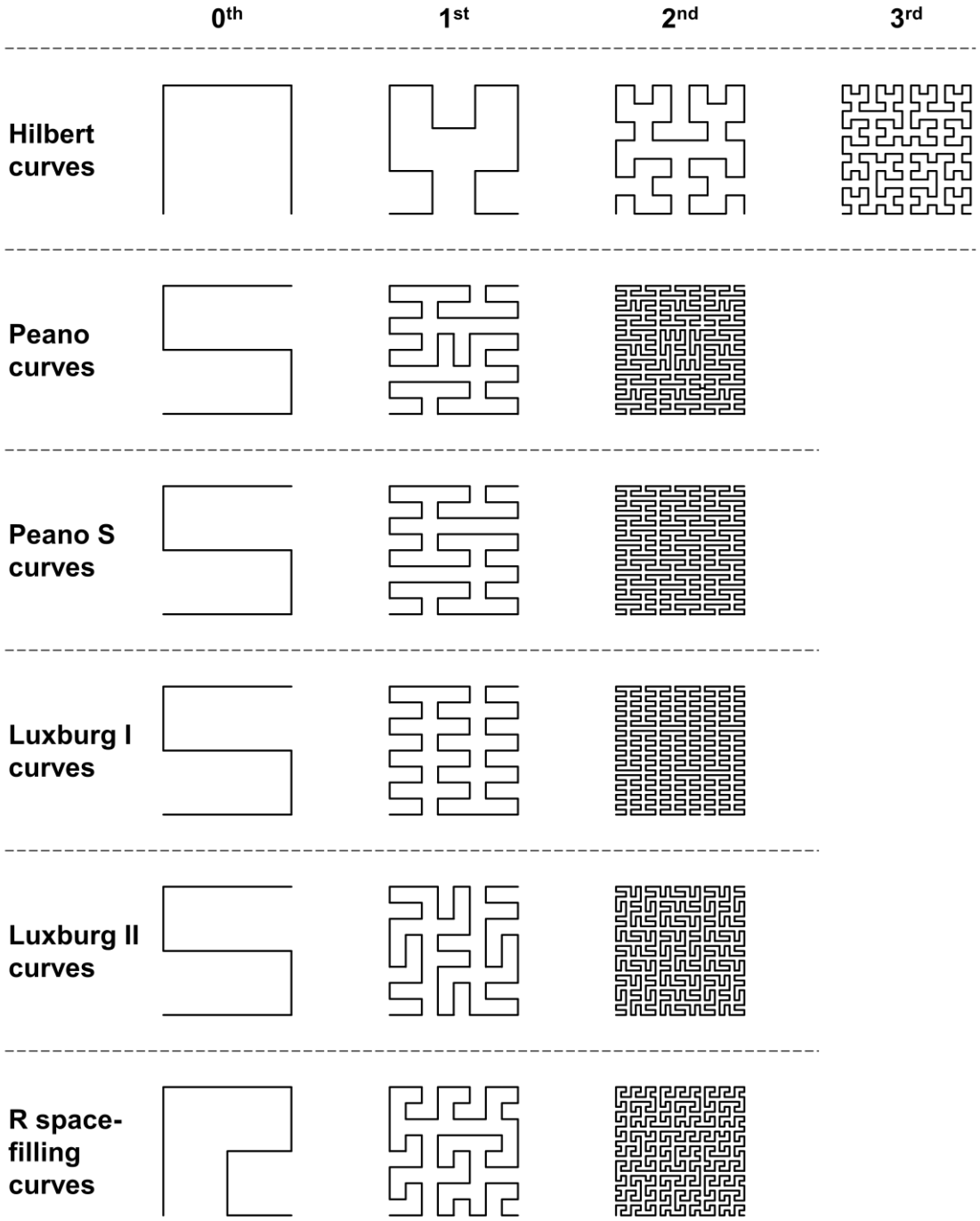

Fig. S2. The fractal designs referred to in this work.

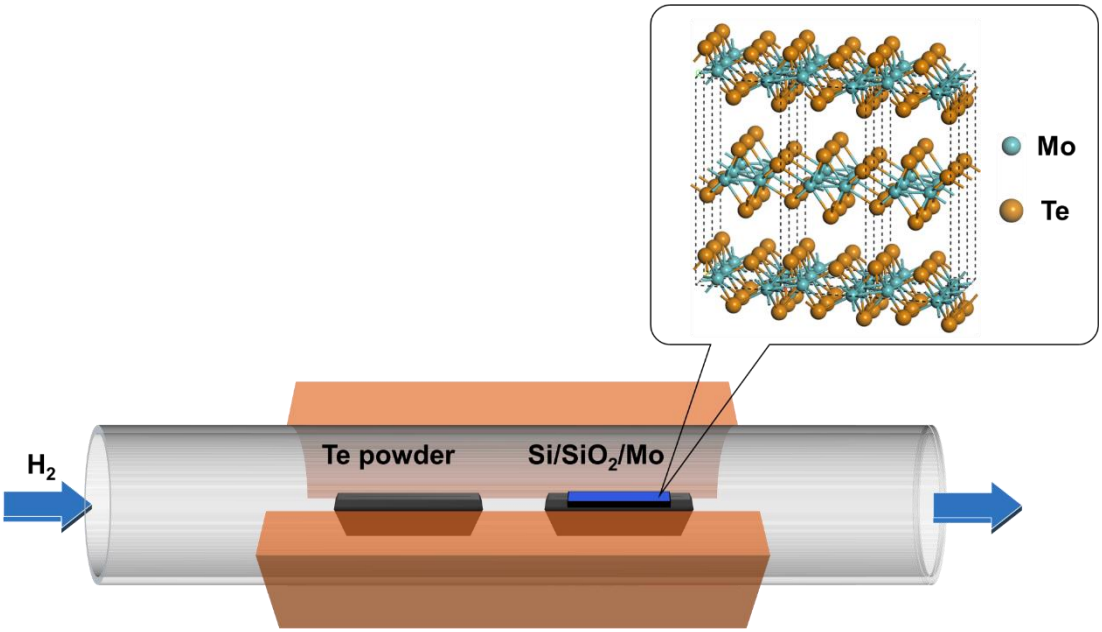

Fig. S3. Scheme of synthesizing 1T'-$MoTe_2$ ultrathin film by a two-zone chemical vapor deposition furnace, and the lattice structure of few-layer 1T'-$MoTe_2$.

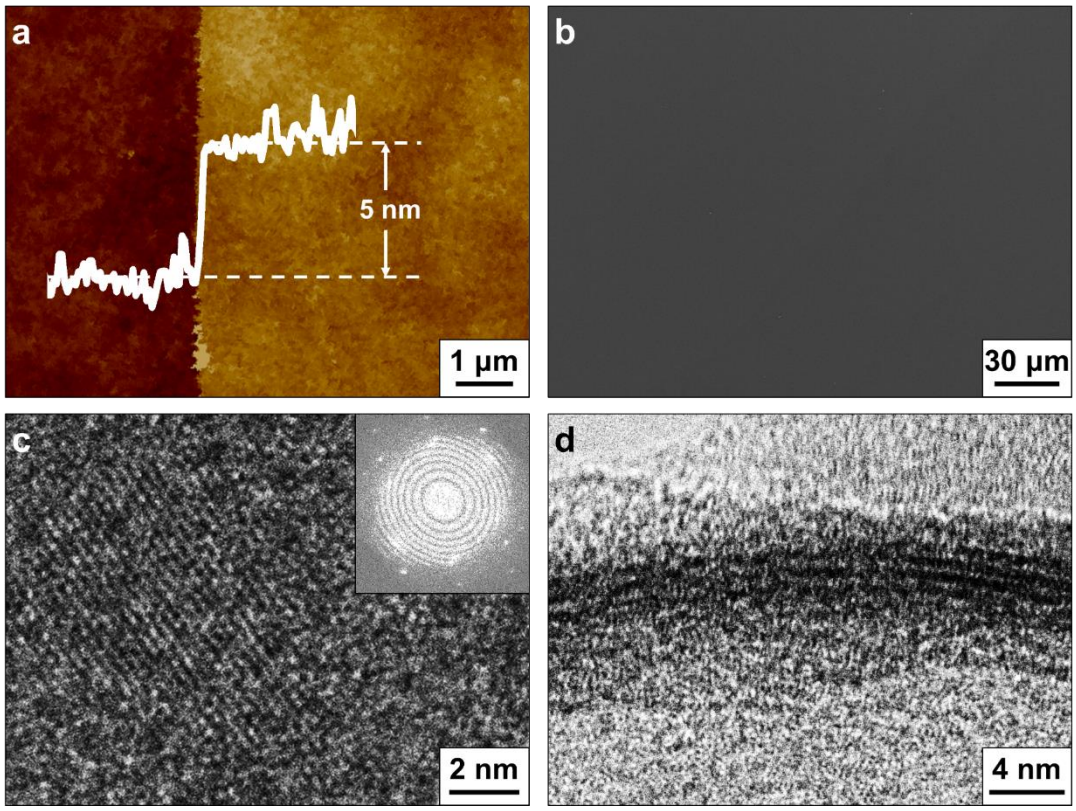

Fig. S4. The morphology and structure of CVD synthesized 1T'-$MoTe_2$ ultrathin film**.** (a) AFM image of the continuous few-layer 1T'-$MoTe_2$ film with an intentionally introduced scratch. The ~5.0 nm thickness of the film can be proven by the height profile of an intentionally introduced scratch, which indicates that the 1T'-$MoTe_2$ film had around 7 layers. (b) SEM image of the surface of 1T'-$MoTe_2$ film. The surface morphology of 1T'-$MoTe_2$ film is extremely smooth without any cracks or winkles. (c) High-resolution TEM image of the basal plane of 1T'-$MoTe_2$ film; inset is the corresponding Fourier transform pattern of the area. 6~8 layers of $MoTe_2$ can be visually counted from the image which corresponds to the AFM result. (d) High-resolution TEM image of the edges of 1T'-$MoTe_2$ film. The interplanar spacing of (001), (100) and (010) are 13.76 Å, 6.27 Å and 3.39 Å as measured, respectively.

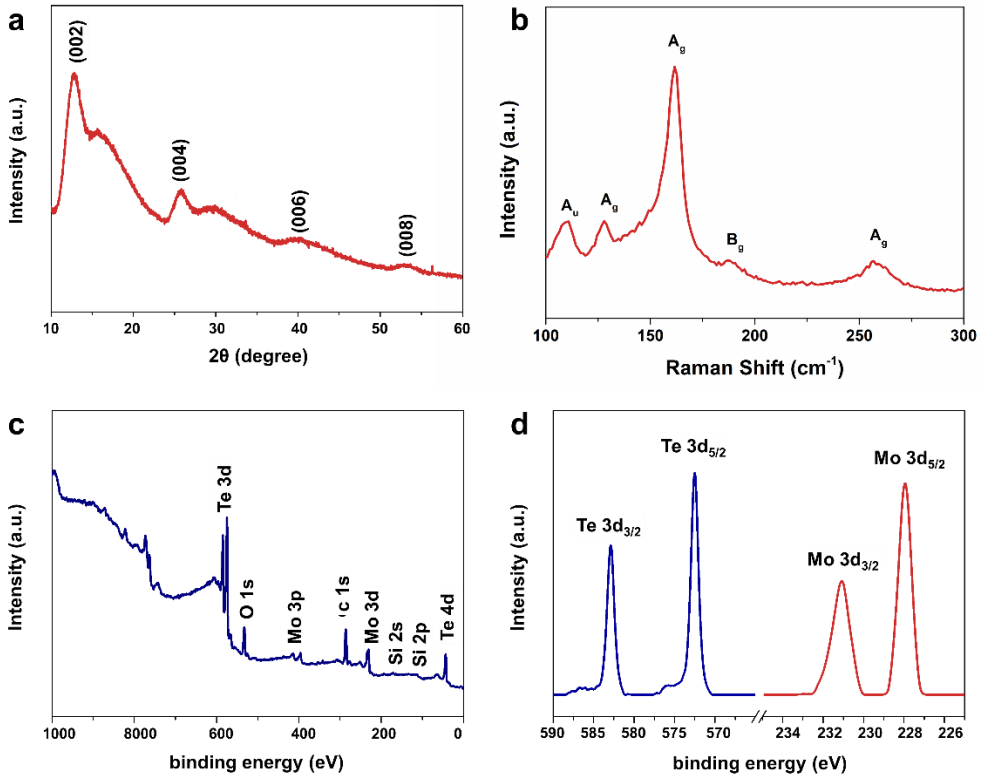

Fig. S5. Characterizations of 1T-$MoTe_2$ film. (a) The XRD patterns of the 1T'-$MoTe_2$ film with distinctive peaks at 2θ = 12.6°, 25.8°, 39.1° and 52.7°, which correspond to the crystal planes of (002), (004), (006) and (008), respectively. (b) Raman spectra of the 1T'-$MoTe_2$ film. Vibration peaks appeared at 109.8 cm^{-1}can be attributed to the A_u mode of 1T'-$MoTe_2$, while the peak located at 127.9, 161.6, 256.9 cm^{-1} corresponded to the A_g mode and 188.4 cm^{-1} corresponded to the B_g mode. (c) XPS spectra of the 1T′-$MoTe_2$ film on Si/SiO_2 substrate. (d) High-resolution Mo 3d and Te 3d XPS spectra of the 1T′-$MoTe_2$ film, respectively. These results confirm each other and prove the successful preparation of few-layer 1T'-$MoTe_2$.

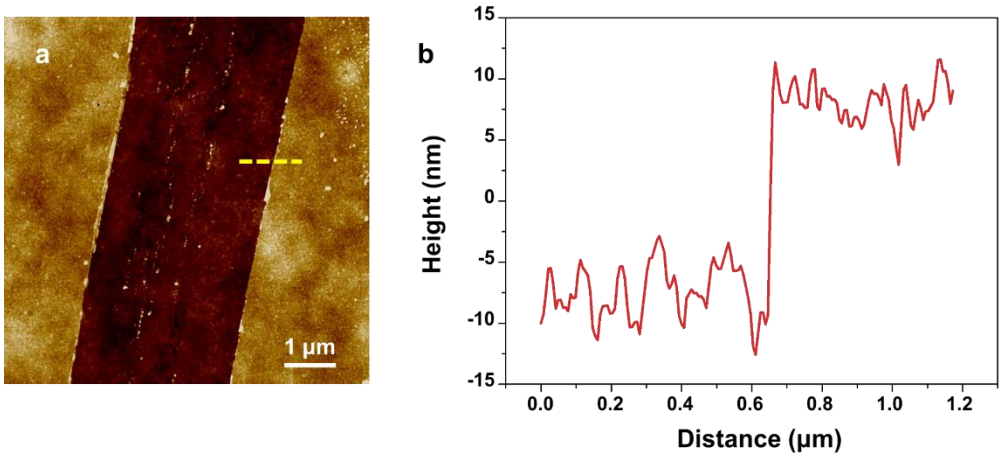

Fig. S6. The thickness of 1T'-$MoTe_2$/Au film on SiO_2/Si substrate. **(**a) AFM image of the 1T'-$MoTe_2$/Au film with an intentionally introduced scratched zone. (b) AFM height profile along the dashed line in (a).

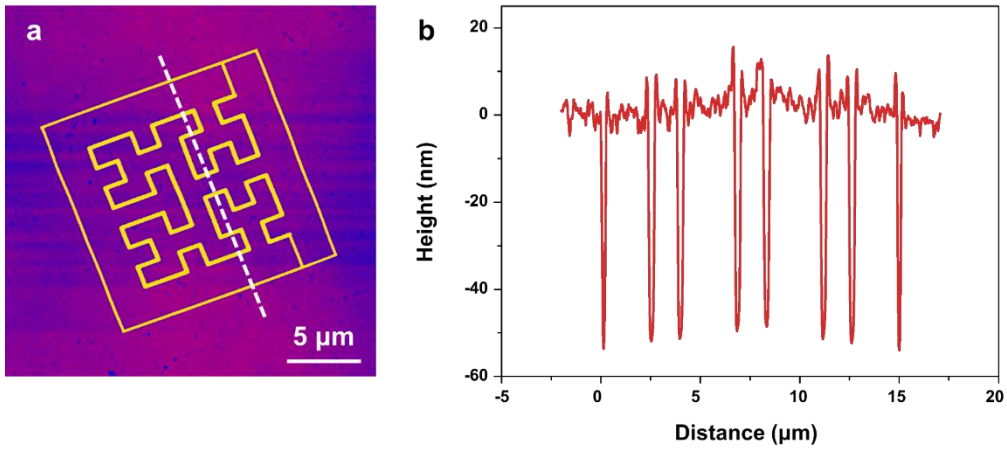

Fig. S7. The depth information of FNSCs. (a) AFM image of the 2nd Hilbert FNSCs with the interspace of 300 nm, where the outline of an NSC can be clearly observed. (b) AFM height profile along the dashed line in (a). The side length of the square device was 15 μm, while the fractal structure was limited to 10 μm. The depths of the fractal structures and boundaries were 50 nm, the same as the value we set on FIB system.

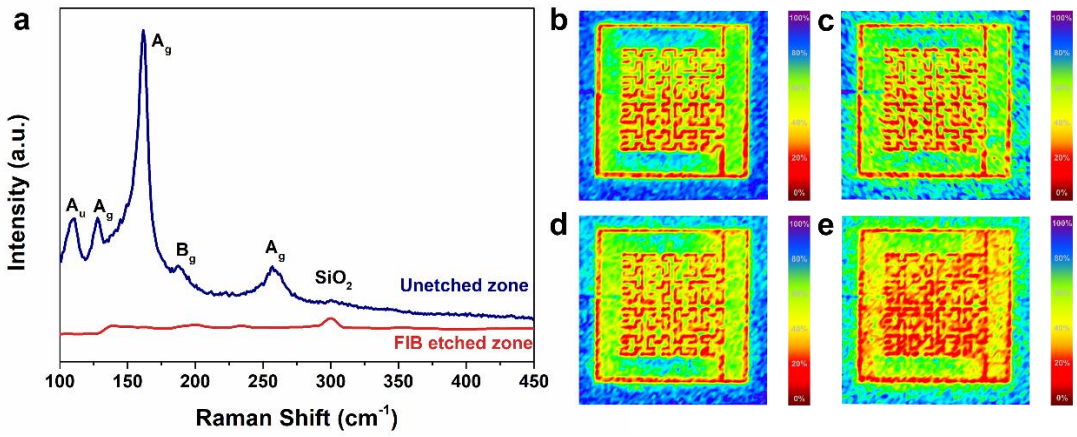

Fig. S8. (a) Raman spectra of the etched zone and unetched zone on 1T'-$MoTe_2$ film corresponding to Fig. 1d. (b-e) The Raman intensity map of a third-order Hilbert FNSC acquired by the percentage intensity of peaks at 109.8 (A_u), 127.9 (A_g), 188.4 (B_g) and 256.9 (A_g) cm^{-1}.

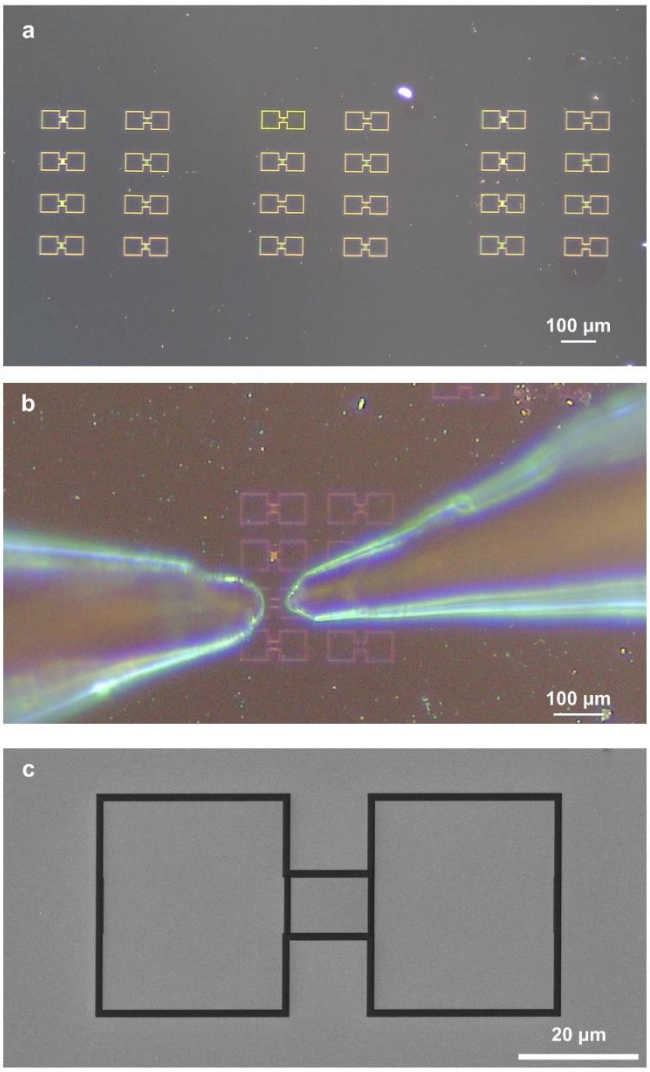

Fig. S9. Optical microscope and SEM images of electrochemical measurement. (a) The FNSCs were prepared to dog-bone shape. (b) The dog-bone shape FNSC was connected to electrochemical workstation through two probes. (c) The extended electrodes to be deduced from the calculation of capacitance performances as the background.

Limited by the size, however, it seemed to be impossible to measure the electrochemical performances of the microcosmic FNSCs by macroscopic instruments. Inspired by the dog-bone shape which is usually used in mechanical testing of materials, two poles of the FNSCs were connected to two larger areas of the film that could be recognized

easily under optical microscope, forming the dog-bone structure. By contacting them with probes, which were mainly encapsulated with nonconducting polymers to minimize the systematical influence, the electrochemical properties including supercapacitor performance can be measured by using an electrochemical workstation. It is worth mentioning that the contribution of the two enlarged areas to the total capacitive performances must be measured and deduced from the calculation of capacitance performances of the FNSCs as the background.

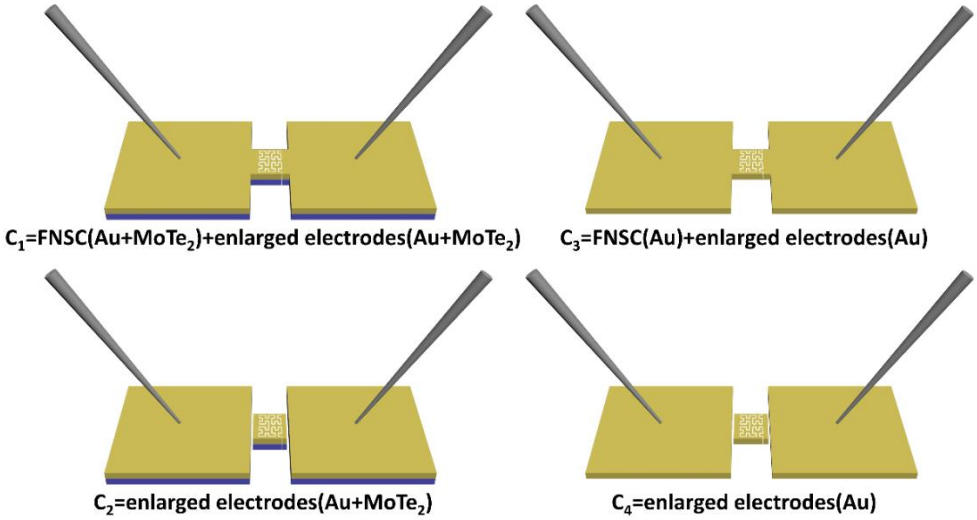

Fig. S10. Schematic diagrams of the capacitances needed to be measured to calculate the contribution of electrode materials of the FNSCs.

In the calculation of one FNSC, 4 capacitances are measured by CV. As shown in Fig. S10, C_1 is the total capacitance of FNSC and the enlarged electrodes with Au and 1T'-$MoTe_2$, C_2 is the capacitance of the enlarged electrodes with Au and 1T'-$MoTe_2$, C_3 is the total capacitance of FNSC and the enlarged electrodes with only Au collector, and C_4 is the capacitance of the enlarged electrodes with only Au collector, respectively. As a result, the capacitance of the FNSC with electrode material 1T'-$MoTe_2$ and Au collector ($C_{FNSC(Au+MoTe_2)}$) is:

$$C_{FNSC(Au+MoTe_2)} = C_1 - C_2$$

Meanwhile, the capacitance of the NSC with only Au collector ($C_{FNSC(Au)}$) is:

$$C_{FNSC(Au)} = C_3 - C_4$$

The final contribution of capacitance of electrode materials 1T'-$MoTe_2$ in the NSC ($C_{FNSC(MoTe_2)}$) is:

$$C_{FNSC(MoTe_2)} = C_{FNSC(Au+MoTe_2)} - C_{FNSC(Au)} = (C_1 - C_2) - (C_3 - C_4)$$

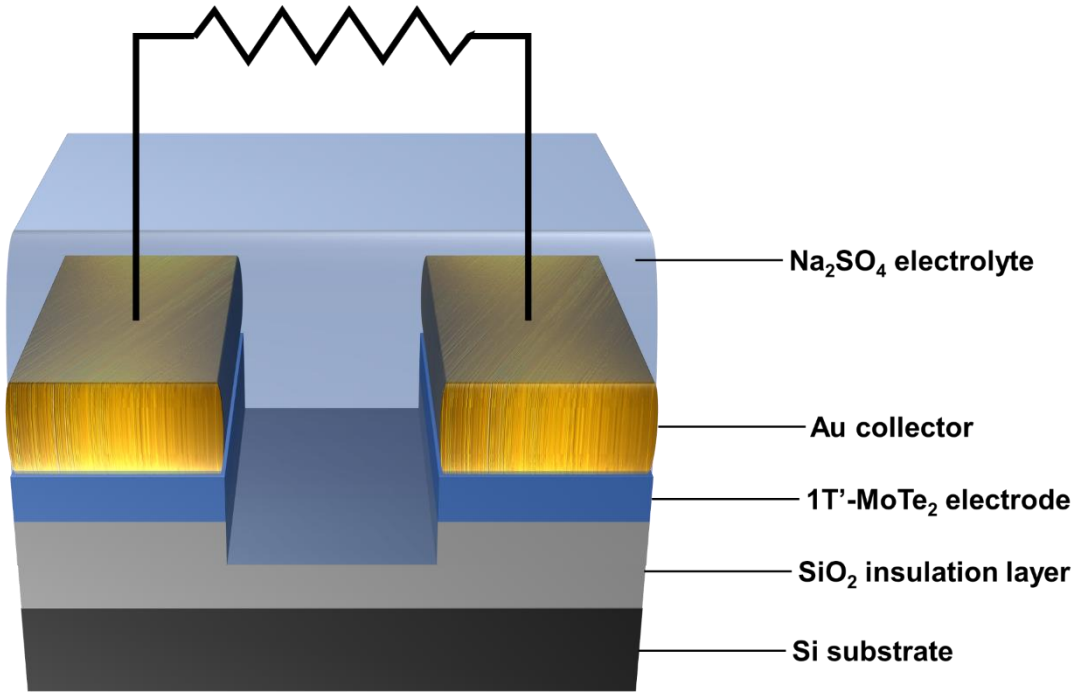

Fig. S11. Schematic illustrations of the FNSC. Cross-sectional diagram of the FNSC including the structures of 1T'-$MoTe_2$ film, Au current collector, SiO_2/Si substrate and Na_2SO_4 electrolyte.

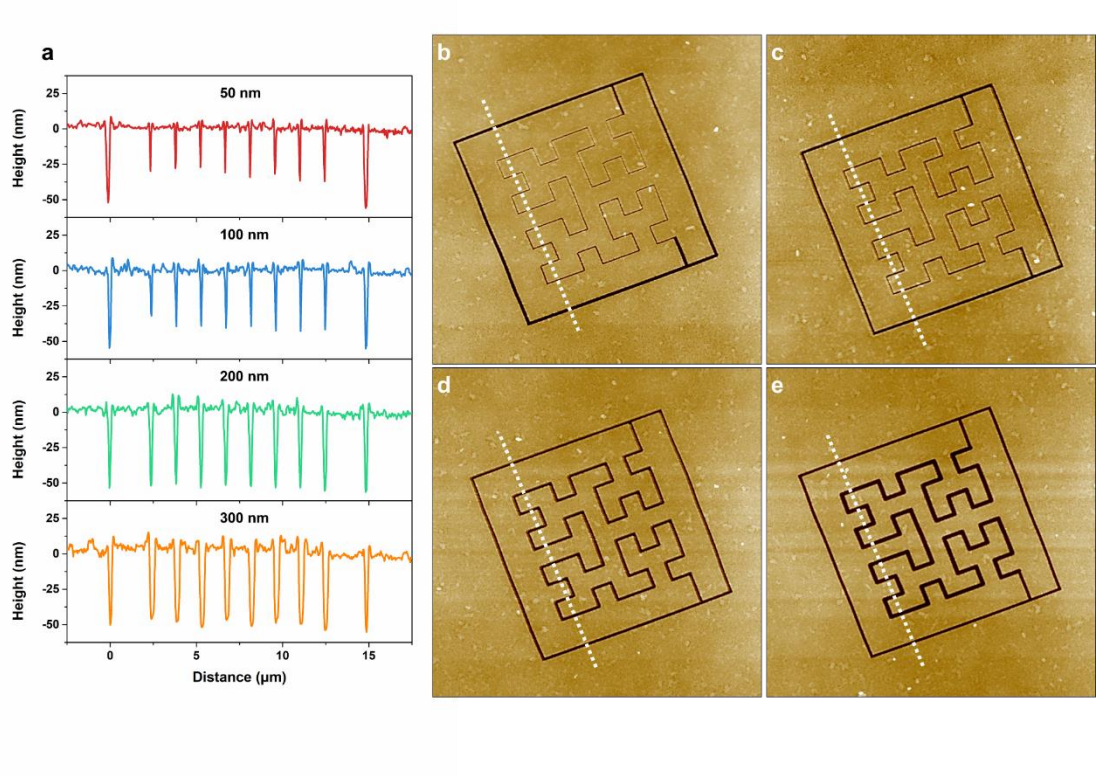

Fig. S12. AFM characterizations of the FNSCs with different interspaces between electrodes. (a) AFM height profiles of the FNSCs with different interspaces between electrodes corresponding to the dashed lines in (b-e). (b-e) 2D AFM images of the FNSCs with the interspaces of 50 nm, 100 nm, 200 nm and 300 nm, respectively. The scalebars are 5 μm.

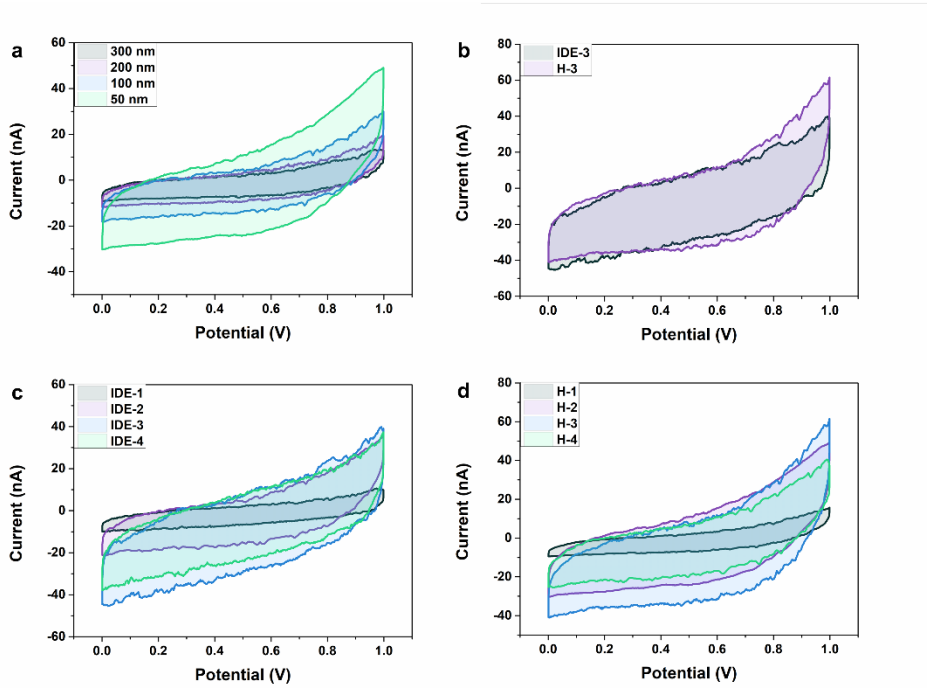

Fig. S13. CV curves at 10 mV/s showing the comparison of different interspaces (a), designs (b) and iterated orders (c-d).

The CV curves at 10 mV/s showing the comparison of different interspaces, iterated orders and designs are plotted in Fig. S13. All the low-scanrate CV curves present no obvious redox peak with a near rectangular shape, indicating the major contribution of fast and reversable electric double layer capacitive process. Besides, there are some small jitters on the curves, which comes from inevitable fluctuations at currents as low as pA. The area enclosed by the curves of different samples demonstrates tendencies which are similar to those of GCD results.

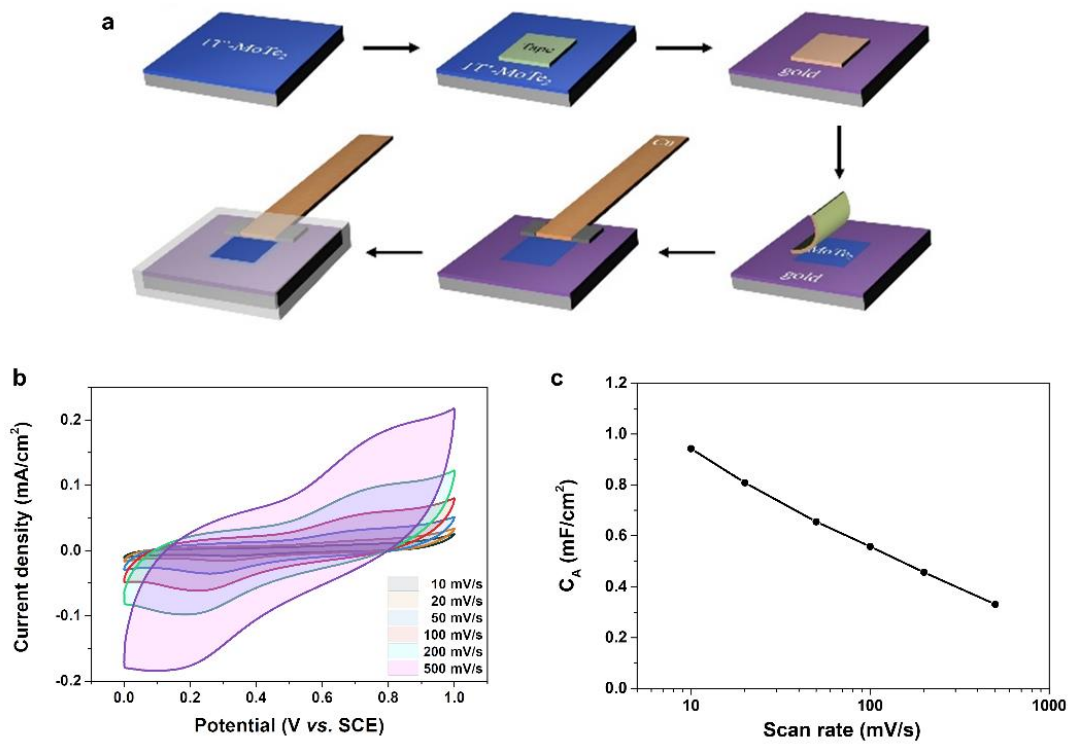

Fig. S14. CV measurements of the 1T'-$MoTe_2$ film in three-electrode system. (a) Preparation of the working electrode of 1T'-$MoTe_2$ film on SiO_2/Si substrate. (b) CV curves of the 1T'-$MoTe_2$ film at rates ranging from 10 to 500 $mV \cdot s^{-1}$. (c) Areal capacitances of the 1T'-$MoTe_2$ film at different scan rates.

Fig. S14a presents the fabrication of the working electrode of 1T'-$MoTe_2$ film. In brief, gold sputtering is performed to reduce the Schottky barrier between few-layer $MoTe_2$ and copper electrode, while a small piece of thermal release tape is used as the mask to leave a clear surface of $MoTe_2$ for CV measurement. The device except for a certain zone is encapsulated by diluted nail polish, which created an exposed area of about 0.5 cm × 0.5 cm, and then tested with a three-electrode system in 1.0 M Na_2SO_4.[1]

Fig. S14b presents the three-electrode CV curves of 1T′-$MoTe_2$ film (*vs.* SCE (saturated calomel electrode)) at various scan rates ranging from 10 to 500 m $V \cdot s^{-1}$ in 1.0 M Na_2SO_4 electrolyte. A pair of strong redox peaks is visible in each voltammogram from

0 to 1.0 V, which represents cation intercalation and reversible redox reactions between different valence states of Mo (+4 and +6), suggesting that the capacitance characteristics are mainly governed by the faradaic redox reaction.[2] The cathodic peaks situated around 0.32 V can be attributed to the electrochemical insertion of Na^+ ions into the interlayer of layered $MoTe_2$. Accordingly, the obvious anodic peaks at 0.70 V correspond to the extraction of Na^+ ions from layered $MoTe_2$. The nearly symmetrical redox peaks of the electrode indicate the high reversibility of the insertion/extraction process. The peak current increases almost linearly with the scan rate, suggesting that the rates of electronic and ionic transportation are quick enough. The areal capacitances of the film are 0.94, 0.66 and 0.33 $mF \cdot cm^{-2}$ at the scan rates of 10, 50 and 500 $mV \cdot s^{-1}$ (Fig. S14c) respectively.

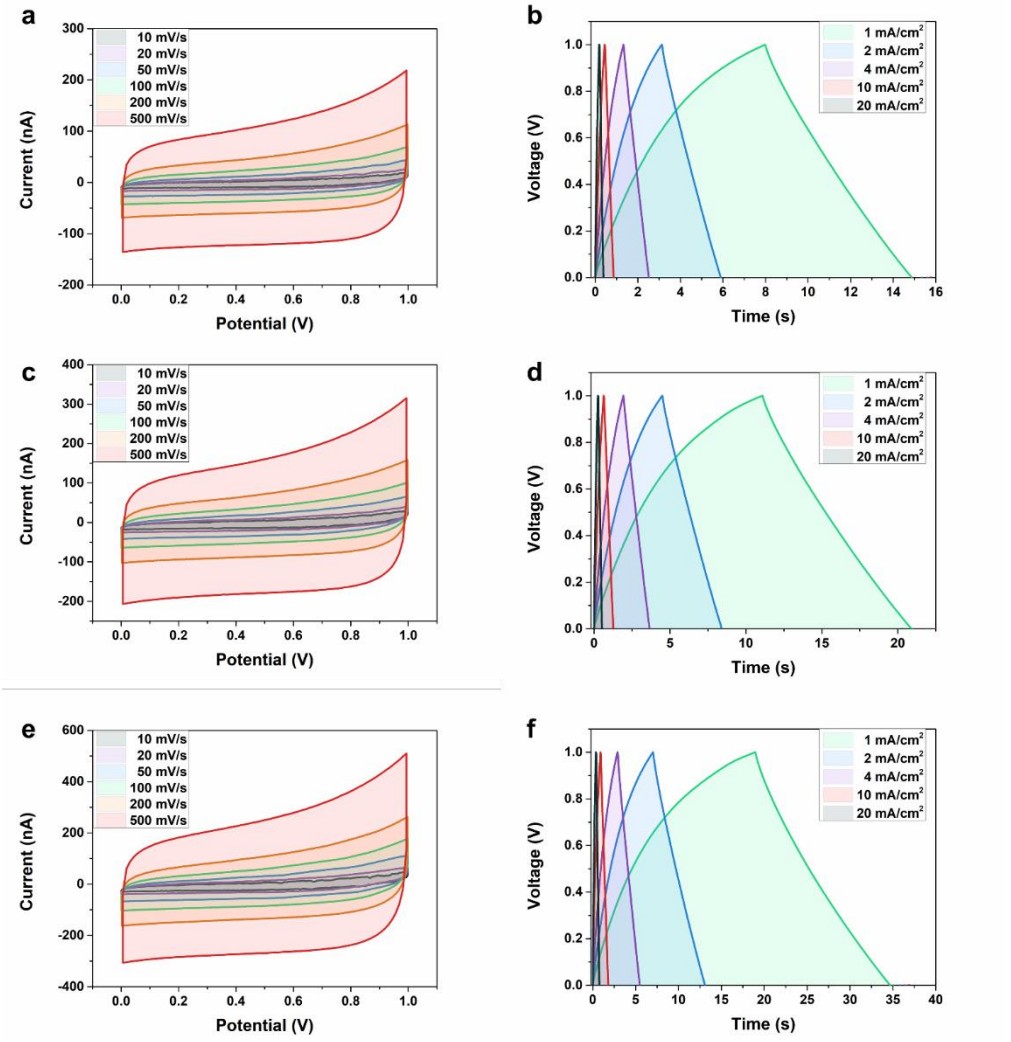

Fig. S15. CV and GCD curves of the 2nd order Hilbert FNSCs with different interspaces between electrodes. a-b) CV (a) and GCD (b) curves of the FNSCs with 200 nm-interspace. (c-d) CV (c) and GCD (d) curves of the FNSCs with 100 nm-interspace. (e-f) CV (e) and GCD (f) curves of the FNSCs with 50 nm-interspace.

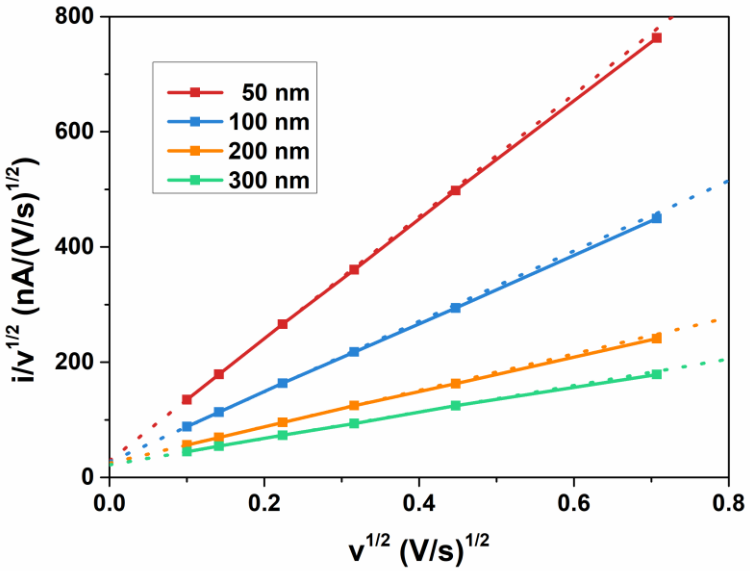

Fig. S16. The plots of $i(V)/v^{1/2}$ versus $v^{1/2}$ of the FNSCs with different interspaces.

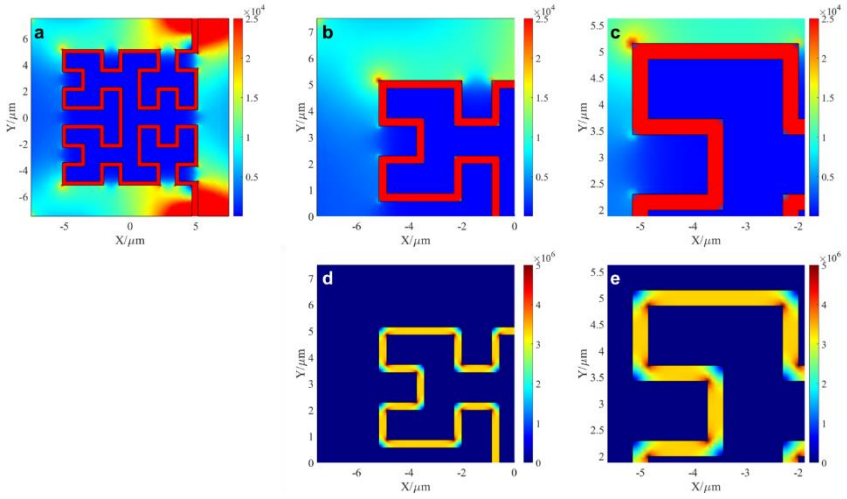

Fig. S17. COMSOL simulations of the electric field intensity distributions (unit: V/m) of the 2nd Hilbert FNSC with 300 nm-interspace. (a) Electric field intensity distribution of the device. (b-c) Partial enlarged views to show the electric filed intensity distribution of the electrodes. (d-e) Partial enlarged views to show the electric filed intensity distribution of 300 nm-interspace.

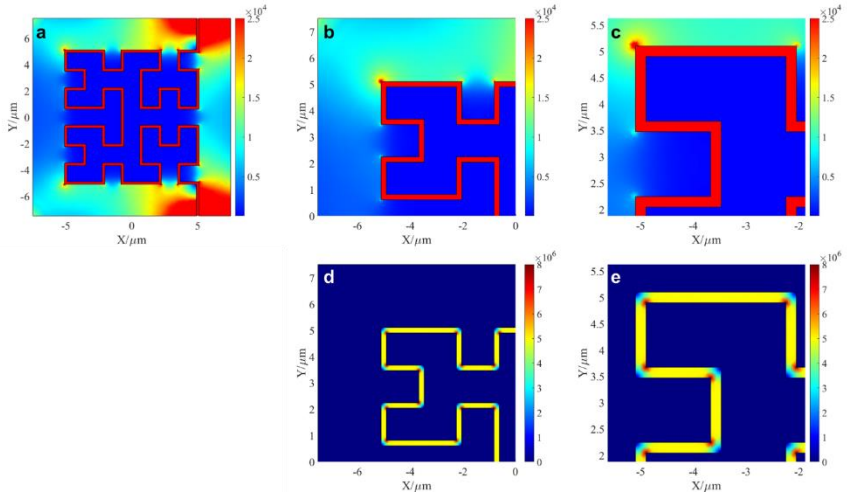

Fig. S18. COMSOL simulations of the electric field intensity distributions (unit: V/m) of the 2nd Hilbert FNSC with 200 nm-interspace. (a) Electric field intensity distribution of the device. (b-c) Partial enlarged views to show the electric filed intensity distribution of the electrodes. (d-e) Partial enlarged views to show the electric filed intensity distribution of 200 nm-interspace.

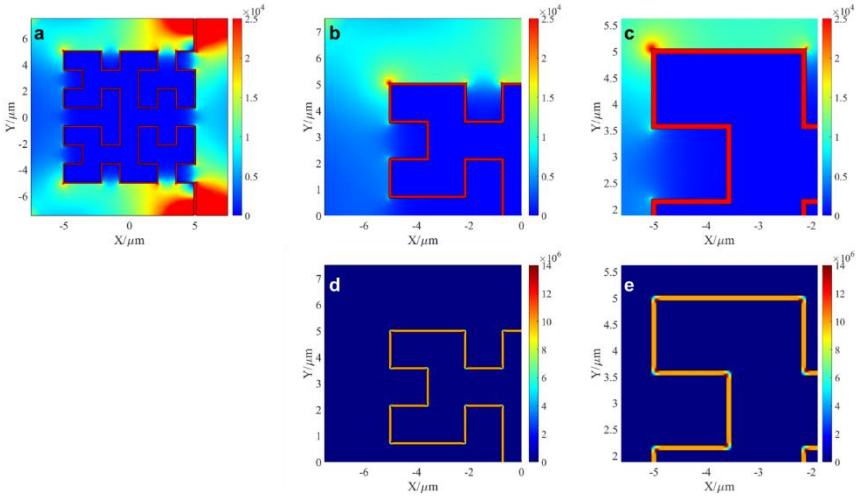

Fig. S19. COMSOL simulations of the electric field intensity distributions (unit: V/m) of the 2nd Hilbert FNSC with 100 nm-interspace. (a) Electric field intensity distribution of the device. (b-c) Partial enlarged views to show the electric filed intensity distribution of the electrodes. (d-e) Partial enlarged views to show the electric filed intensity distribution of 100 nm-interspace.

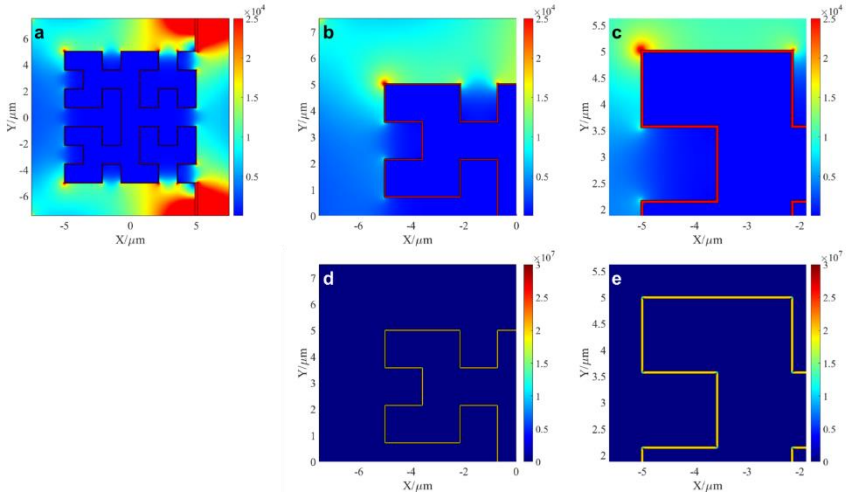

Fig. S20. COMSOL simulations of the electric field intensity distributions (unit: V/m) of the 2nd Hilbert FNSC with 50 nm-interspace. (a) Electric field intensity distribution of the device. (b-c) Partial enlarged views to show the electric filed intensity distribution of the electrodes. (d-e) Partial enlarged views to show the electric filed intensity distribution of 50 nm-interspace.

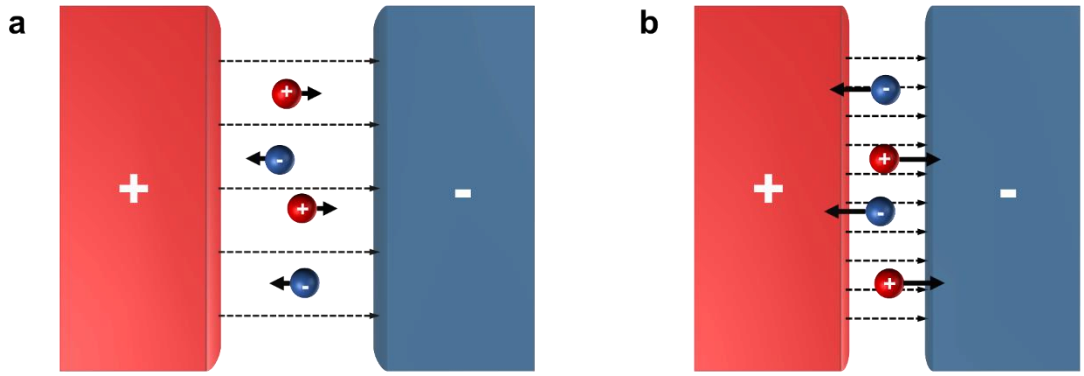

Fig. S21. (a) Schematic diagrams of electrolyte ions effected by weak electric field force among big interspace. (b) Effected by strong electric field force among small interspace. (dashed arrow: electric field line; solid arrow: electric field force.)

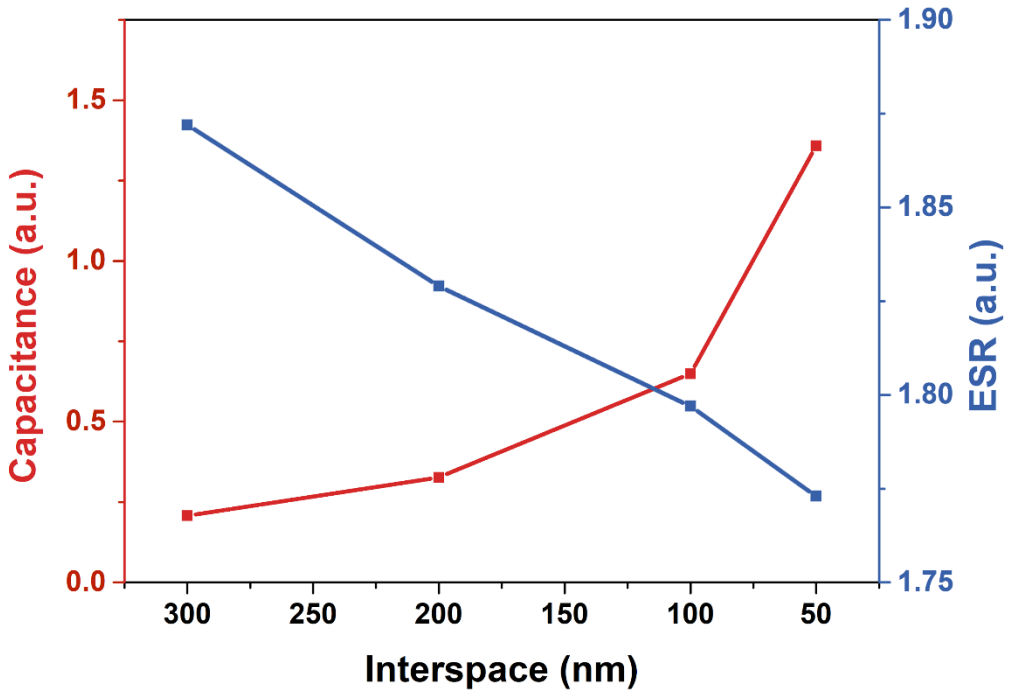

Fig. S22. COMSOL simulated capacitances and ESRs of the 2nd Hilbert FNSCs with different interspaces.

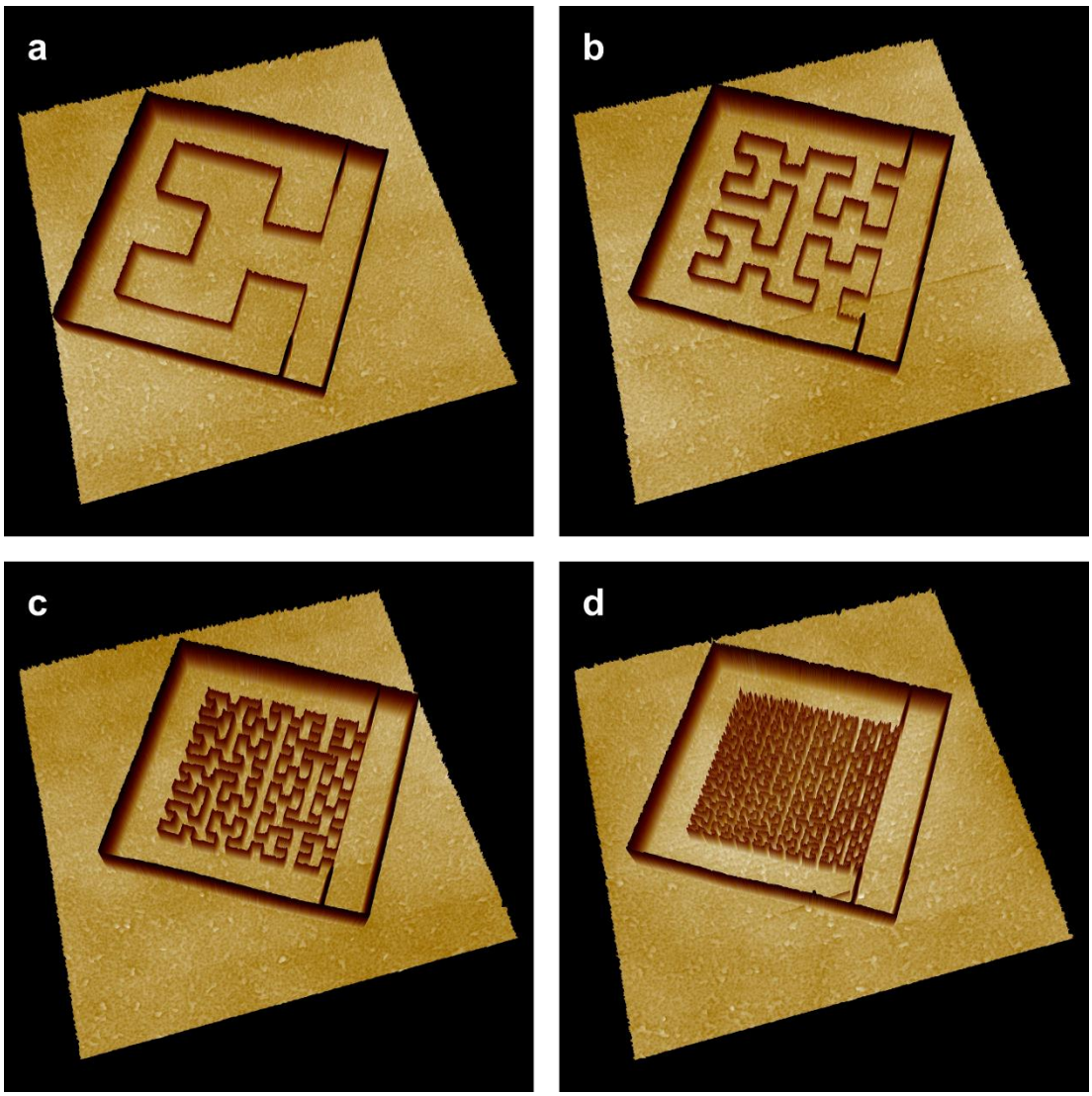

Fig. S23. Bottom view of the 3D AFM images of the 1st (a), 2nd (b), 3rd (c) and 4th (d) Hilbert fractal designed devices with the side length of 15 μm.

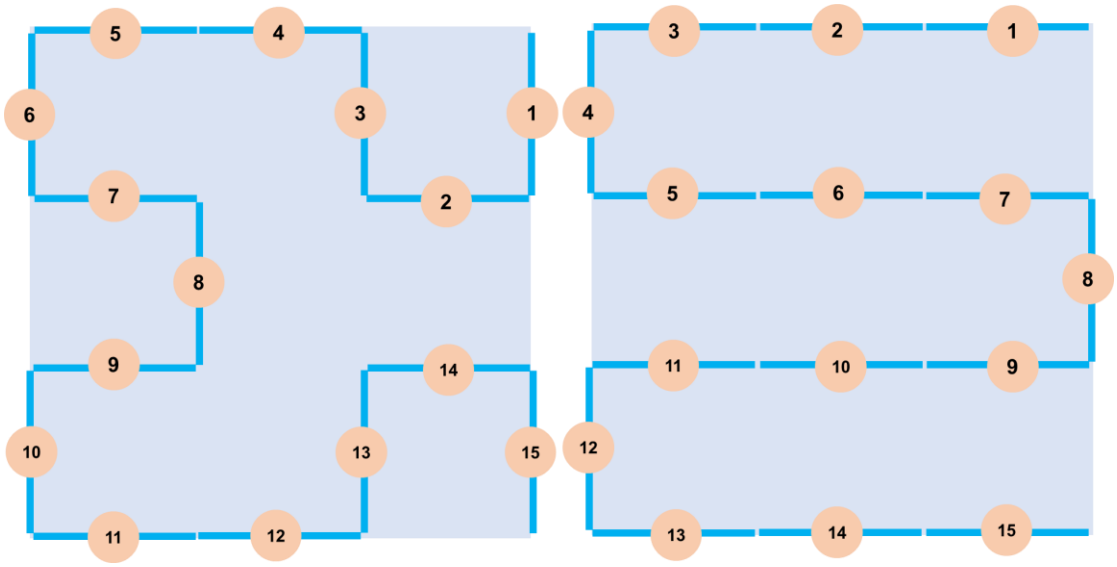

Fig. S24. Illustration of the length of fractal and IDE curves of the same iterated order.

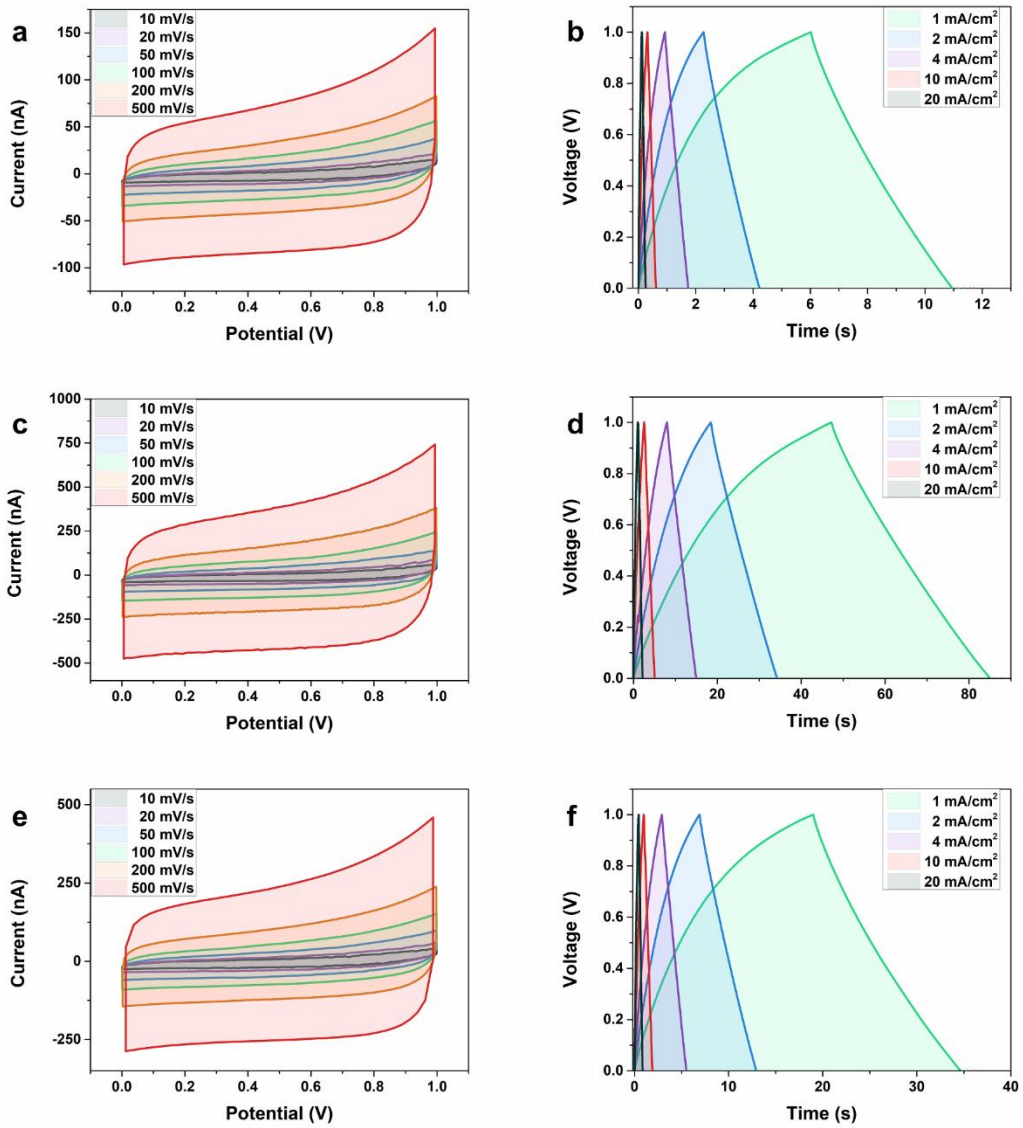

Fig. S25. CV and GCD curves of the FNSCs with different iterated orders of Hilbert fractal designs with the interspaces of 50 nm. (a-b) CV (a) and GCD (b) curves of **H-1** FNSCs. (c-d) CV (c) and GCD (d) curves of **H-3** FNSCs. (e-f) CV (e) and GCD (f) curves of **H-4** FNSCs. CV and GCD curves of **H-2** FNSCs with the interspaces of 50 nm are shown in Fig. S14.

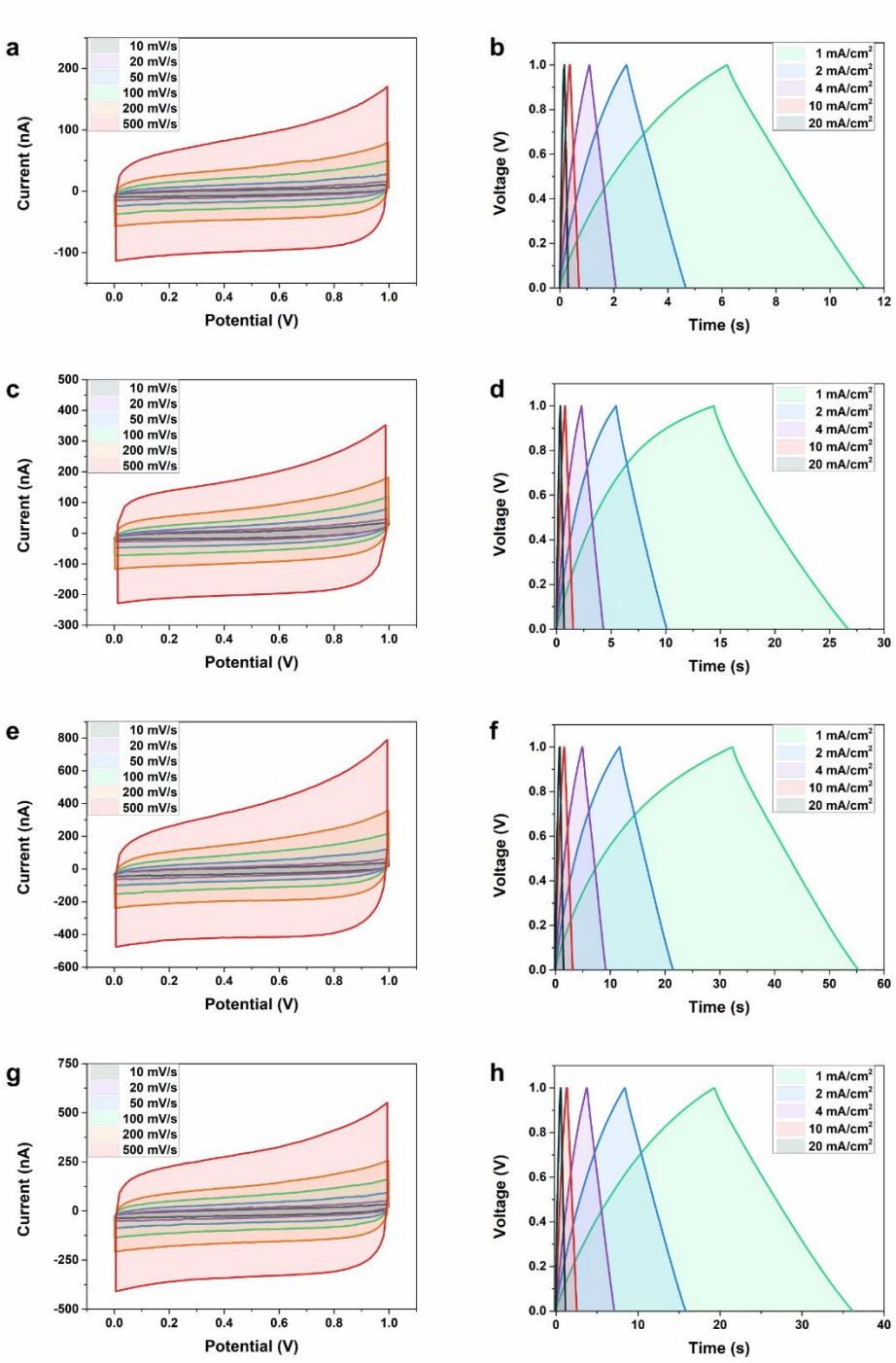

Fig. S26. CV and GCD curves of the IDE NSCs corresponding to different iterated orders of Hilbert fractal designs with the interspaces of 50 nm. (a-b) CV (a) and GCD (b) curves of **IDE-1** NSCs. (c-d) CV (c) and GCD (d) curves of **IDE-2** NSCs. (e-f) CV (e) and GCD (f) curves of **IDE-3** NSCs. (g-h) CV (g) and GCD (h) curves of **IDE-4** NSCs.

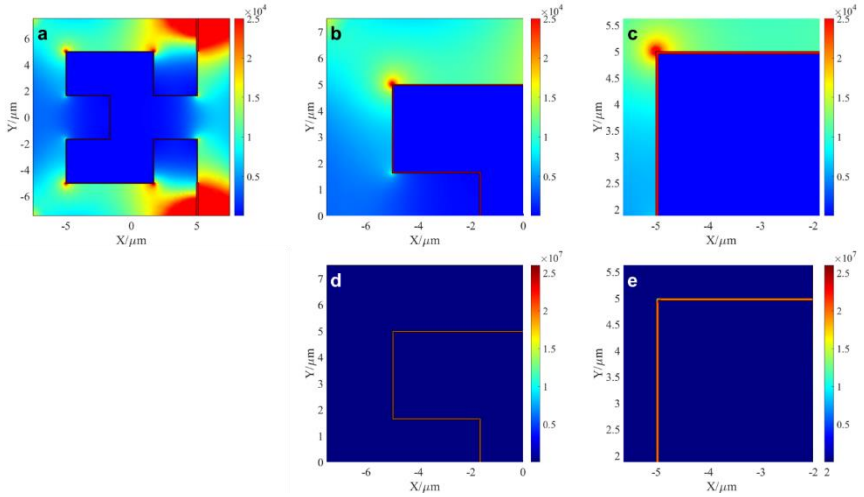

Fig. S27. COMSOL simulations of the electric field intensity distributions (unit: V/m) of the H-1 FNSC with 50 nm-interspace. (a) Electric field intensity distribution of the device. (b-c) Partial enlarged views to show the electric filed intensity distribution of the electrodes. (d-e) Partial enlarged views to show the electric filed intensity distribution of 50 nm-interspace.

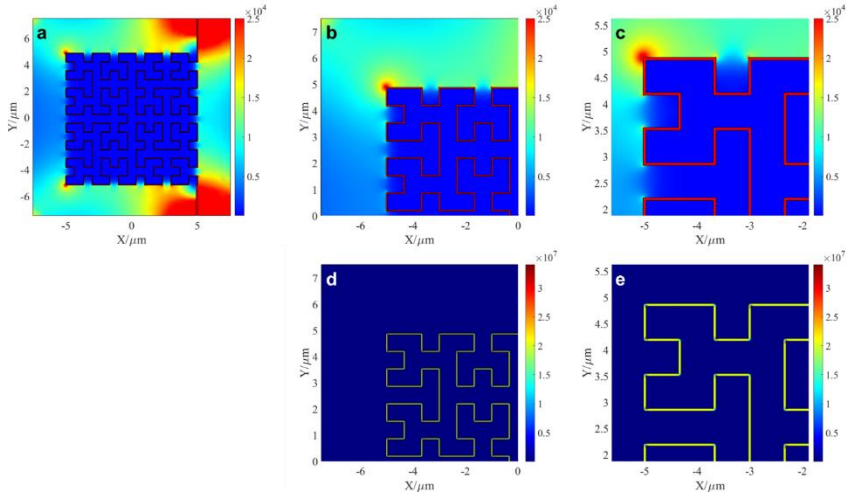

Fig. S28. COMSOL simulations of the electric field intensity distributions (unit: V/m) of the H-3 FNSC with 50 nm-interspace. (a) Electric field intensity distribution of the device. (b-c) Partial enlarged views to show the electric filed intensity distribution of the electrodes. (d-e) Partial enlarged views to show the electric filed intensity distribution of 50 nm-interspace.

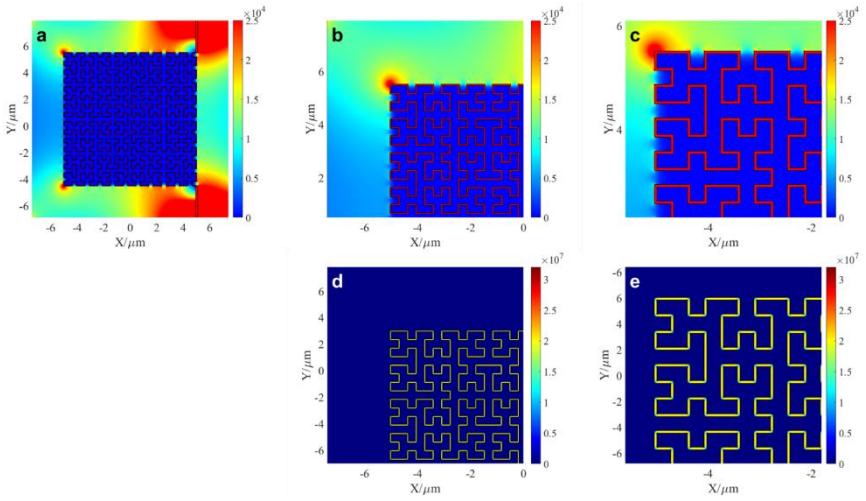

Fig. S29. COMSOL simulations of the electric field intensity distributions (unit: V/m) of the H-4 FNSC with 50 nm-interspace. (a) Electric field intensity distribution of the device. (b-c) Partial enlarged views to show the electric filed intensity distribution of the electrodes. (d-e) Partial enlarged views to show the electric filed intensity distribution of 50 nm-interspace.

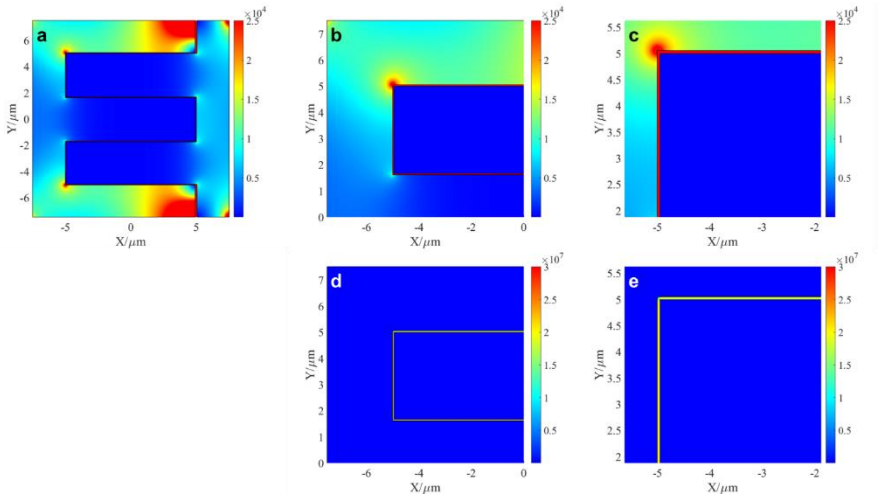

Fig. S30. COMSOL simulations of the electric field intensity distributions (unit: V/m) of the IDE-1 NSC with 50 nm-interspace. (a) Electric field intensity distribution of the device. (b-c) Partial enlarged views to show the electric filed intensity distribution of the electrodes. (d-e) Partial enlarged views to show the electric filed intensity distribution of 50 nm-interspace.

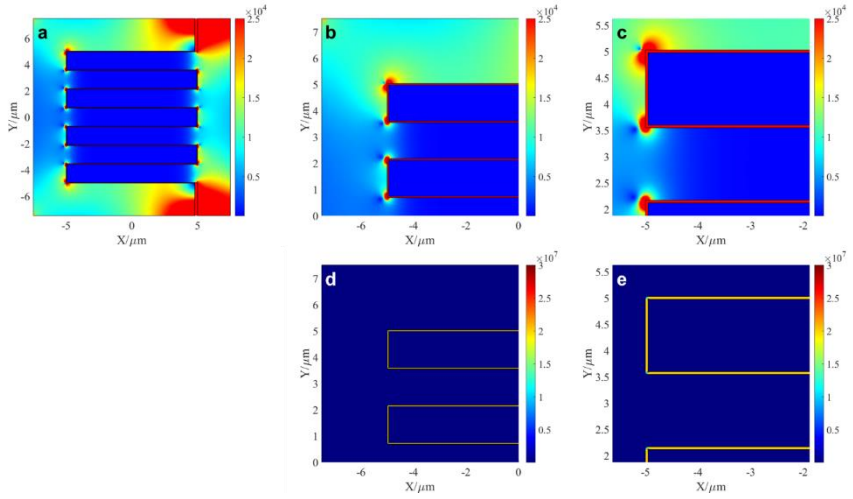

Fig. S31. COMSOL simulations of the electric field intensity distributions (unit: V/m) of the IDE-2 NSC with 50 nm-interspace. (a) Electric field intensity distribution of the device. (b-c) Partial enlarged views to show the electric filed intensity distribution of the electrodes. (d-e) Partial enlarged views to show the electric filed intensity distribution of 50 nm-interspace.

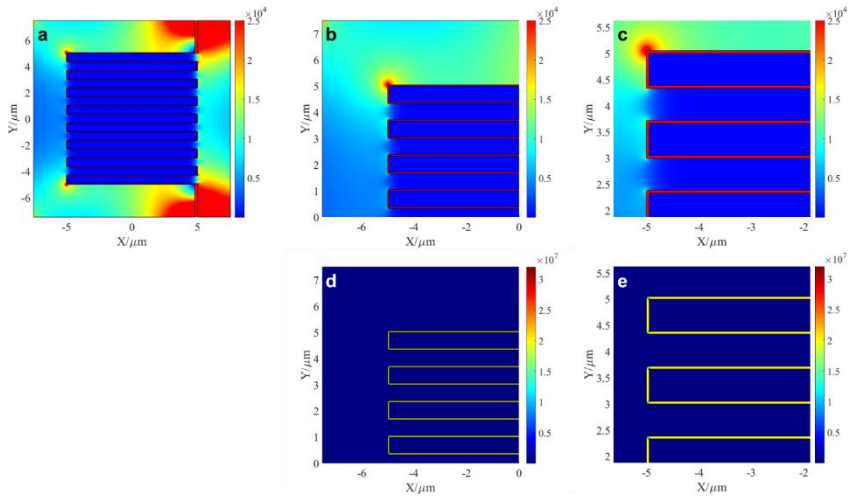

Fig. S32. COMSOL simulations of the electric field intensity distributions (unit: V/m) of the IDE-3 NSC with 50 nm-interspace. (a) Electric field intensity distribution of the device. (b-c) Partial enlarged views to show the electric filed intensity distribution of the electrodes. (d-e) Partial enlarged views to show the electric filed intensity distribution of 50 nm-interspace.

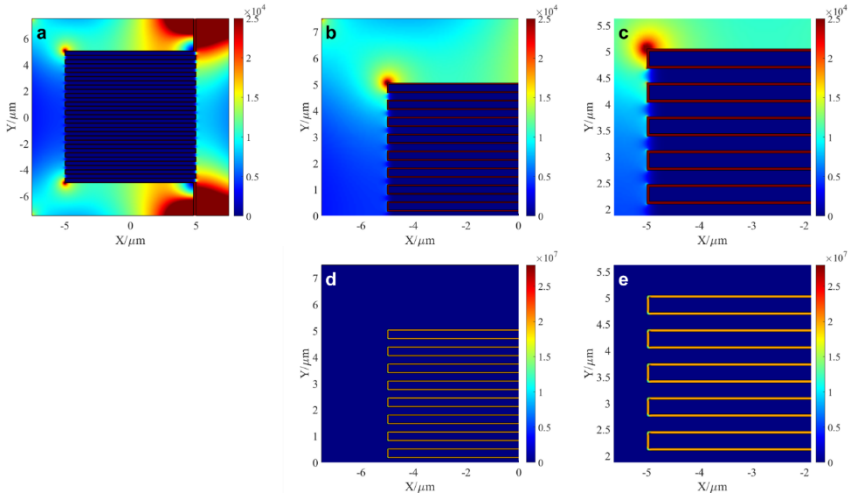

Fig. S33. COMSOL simulations of the electric field intensity distributions (unit: V/m) of the IDE-4 NSC with 50 nm-interspace. (a) Electric field intensity distribution of the device. (b-c) Partial enlarged views to show the electric filed intensity distribution of the electrodes. (d-e) Partial enlarged views to show the electric filed intensity distribution of 50 nm-interspace.

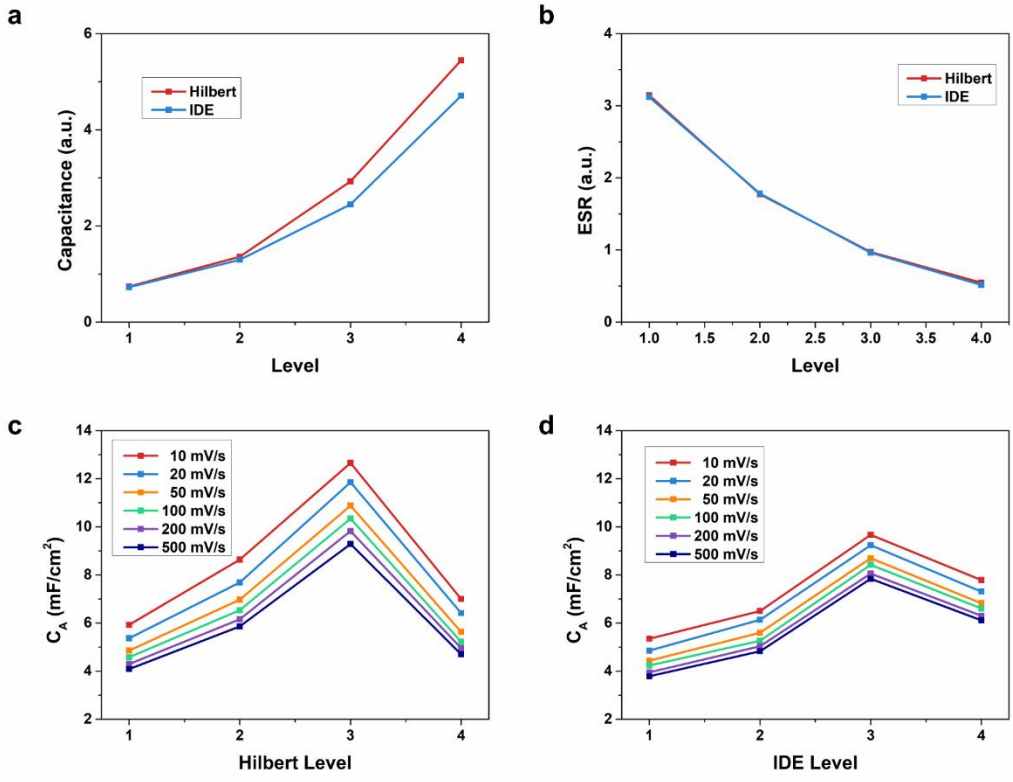

Fig. S34. (a-b) COMSOL simulated capacitances (a) and ESRs (b) of the fractal designs and IDE designs NSCs with different iterated orders. (c-d) Measured results of areal capacitances of the fractal designs (c) and IDE designs (d) NSCs with different iterated orders.

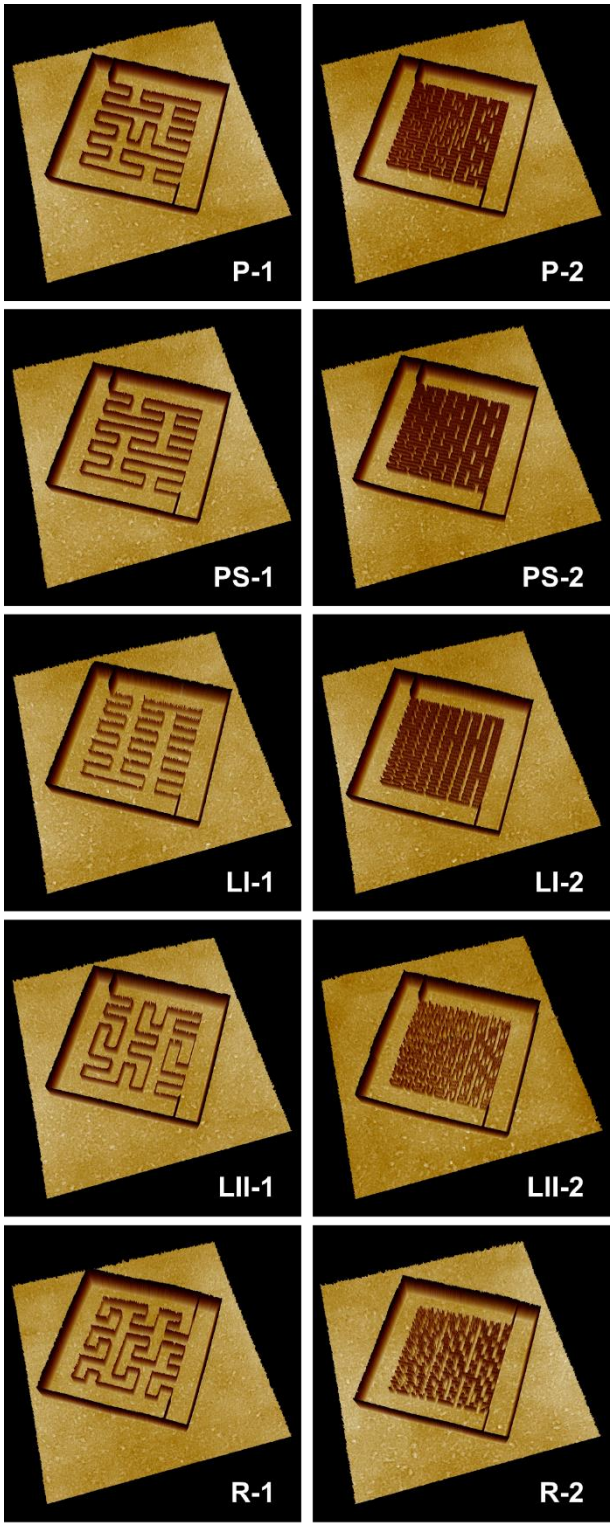

Fig. S35. Bottom view of the 3D AFM images of the FNSCs with the side length of 15 μm.

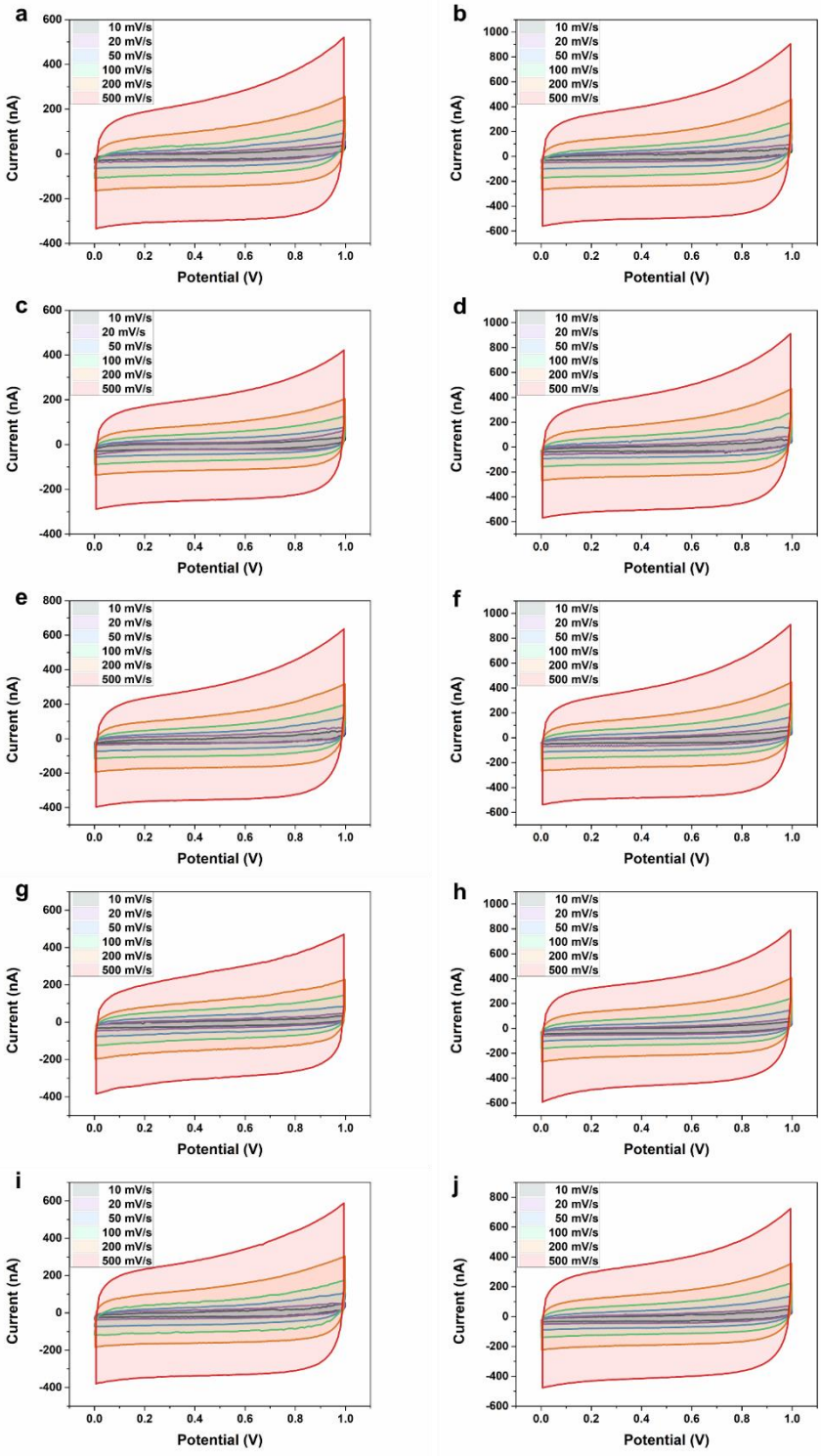

Fig. S36. CV curves of the FNSCs with different iterated orders of fractal designs with the interspaces of 50 nm. (a) P-1. (b) P-2. (c) PS-1. (d) PS-2. (e) LI-1. (f) LI-2. (g) LII-1. (h) LII-2. (i) R-1. (j) R-2.

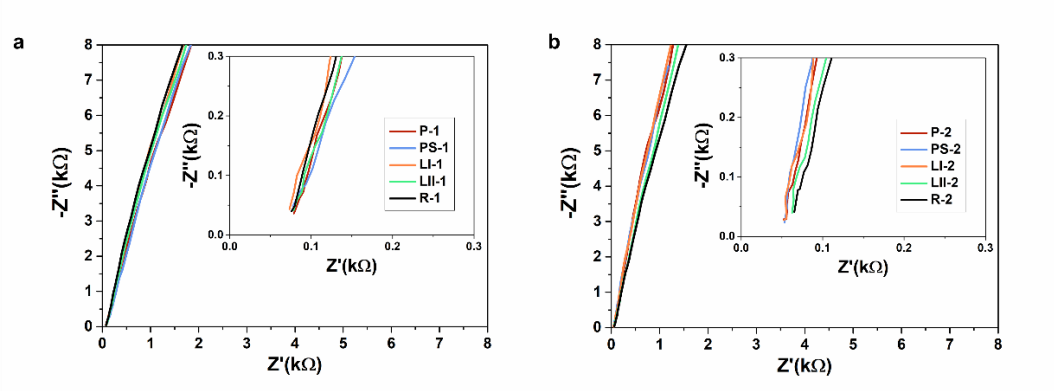

Fig. S37. Impedance spectra (inset is the zoom-in view in the high frequency region) of the FNSCs with different pattern designs.

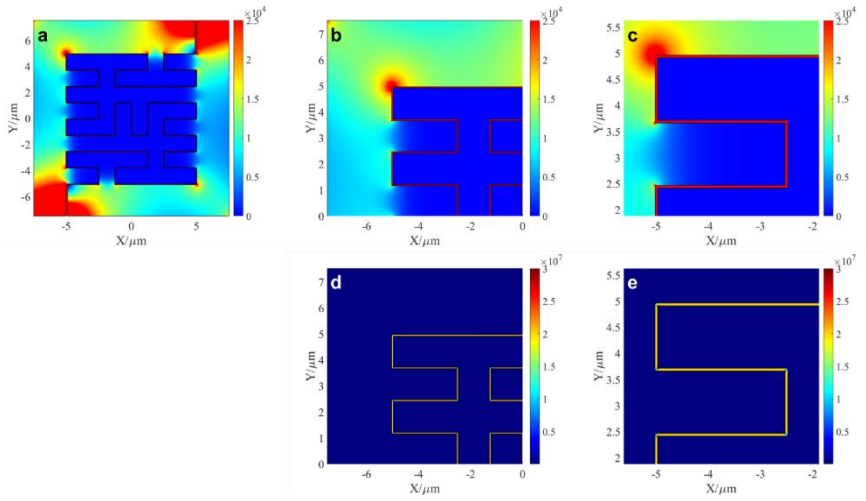

Fig. S38. COMSOL simulations of the electric field intensity distributions (unit: V/m) of the P-1 FNSC with 50 nm-interspace. (a) Electric field intensity distribution of the device. (b-c) Partial enlarged views to show the electric filed intensity distribution of the electrodes. (d-e) Partial enlarged views to show the electric filed intensity distribution of 50 nm-interspace.

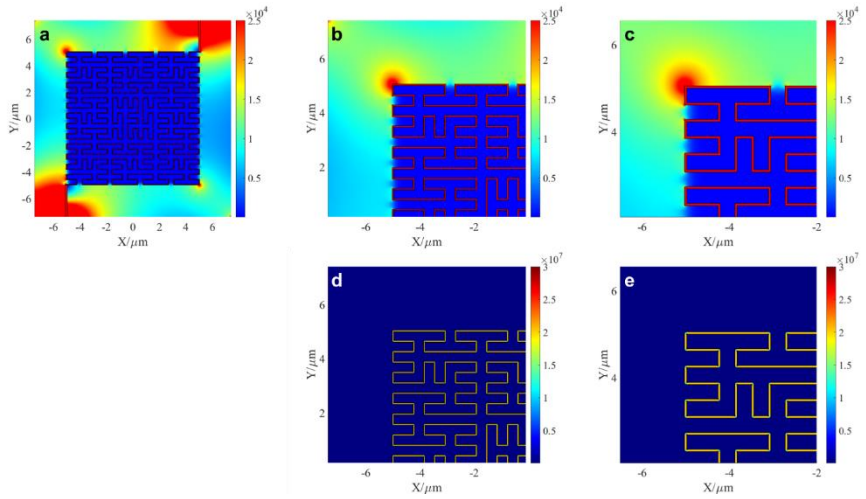

Fig. S39. COMSOL simulations of the electric field intensity distributions (unit: V/m) of the P-2 FNSC with 50 nm-interspace. (a) Electric field intensity distribution of the device. (b-c) Partial enlarged views to show the electric filed intensity distribution of the electrodes. (d-e) Partial enlarged views to show the electric filed intensity distribution of 50 nm-interspace.

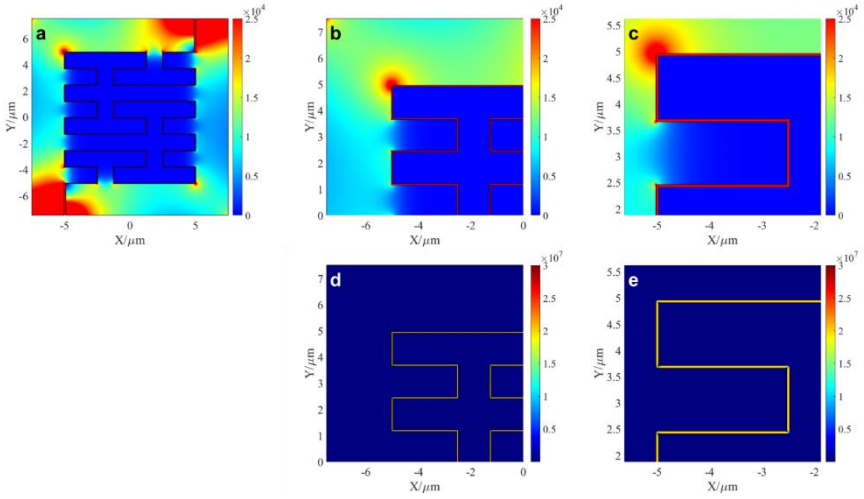

Fig. S340. COMSOL simulations of the electric field intensity distributions (unit: V/m) of the PS-1 FNSC with 50 nm-interspace. (a) Electric field intensity distribution of the device. (b-c) Partial enlarged views to show the electric filed intensity distribution of the electrodes. (d-e) Partial enlarged views to show the electric filed intensity distribution of 50 nm-interspace.

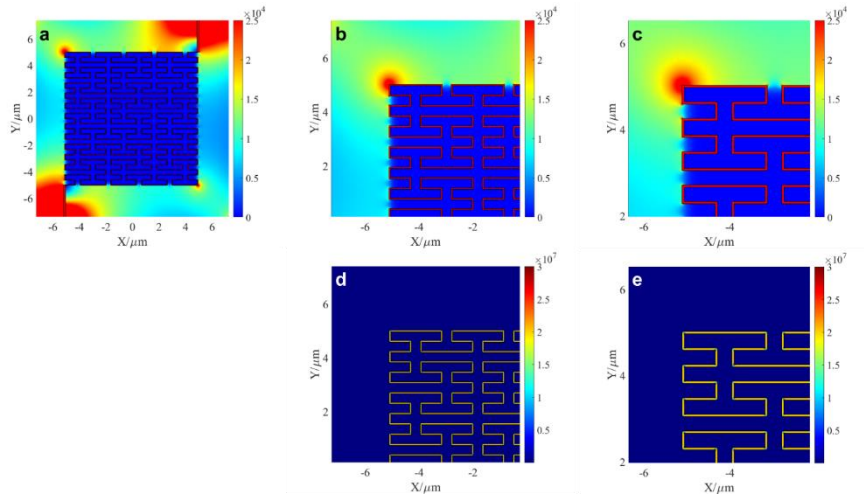

Fig. S41. COMSOL simulations of the electric field intensity distributions (unit: V/m) of the PS-2 FNSC with 50 nm-interspace. (a) Electric field intensity distribution of the device. (b-c) Partial enlarged views to show the electric filed intensity distribution of the electrodes. (d-e) Partial enlarged views to show the electric filed intensity distribution of 50 nm-interspace.

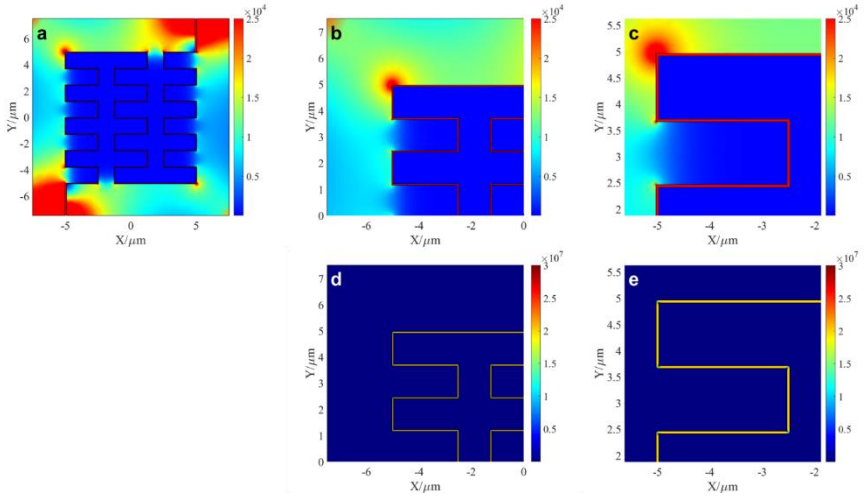

Fig. S42. COMSOL simulations of the electric field intensity distributions (unit: V/m) of the LI-1 FNSC with 50 nm-interspace. (a) Electric field intensity distribution of the device. (b-c) Partial enlarged views to show the electric filed intensity distribution of the electrodes. (d-e) Partial enlarged views to show the electric filed intensity distribution of 50 nm-interspace.

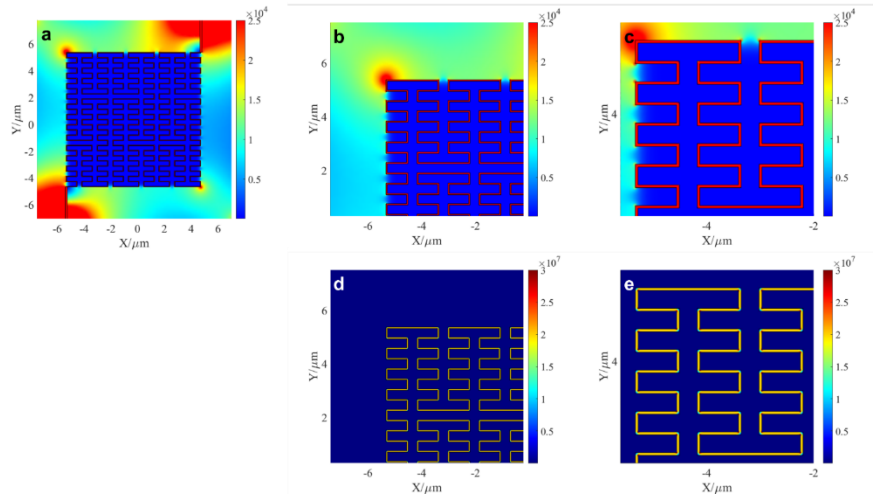

Fig. S43. COMSOL simulations of the electric field intensity distributions (unit: V/m) of the LI-2 FNSC with 50 nm-interspace. (a) Electric field intensity distribution of the device. (b-c) Partial enlarged views to show the electric filed intensity distribution of the electrodes. (d-e) Partial enlarged views to show the electric filed intensity distribution of 50 nm-interspace.

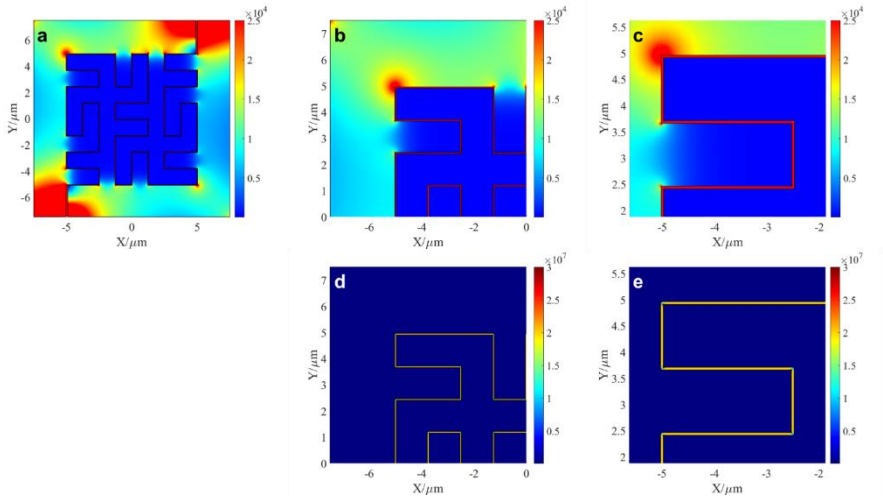

Fig. S44. COMSOL simulations of the electric field intensity distributions (unit: V/m) of the LII-1 FNSC with 50 nm-interspace. (a) Electric field intensity distribution of the device. (b-c) Partial enlarged views to show the electric filed intensity distribution of the electrodes. (d-e) Partial enlarged views to show the electric filed intensity distribution of 50 nm-interspace.

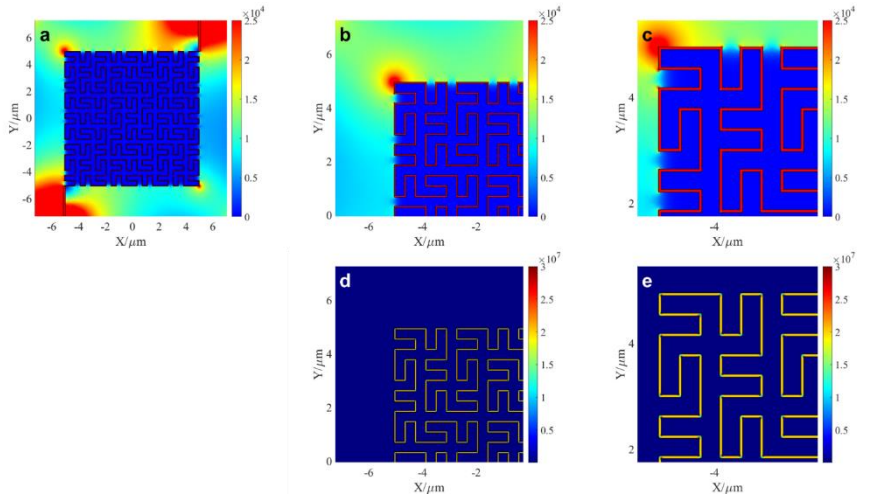

Fig. S45. COMSOL simulations of the electric field intensity distributions (unit: V/m) of the LII-2 FNSC with 50 nm-interspace. (a) Electric field intensity distribution of the device. (b-c) Partial enlarged views to show the electric filed intensity distribution of the electrodes. (d-e) Partial enlarged views to show the electric filed intensity distribution of 50 nm-interspace.

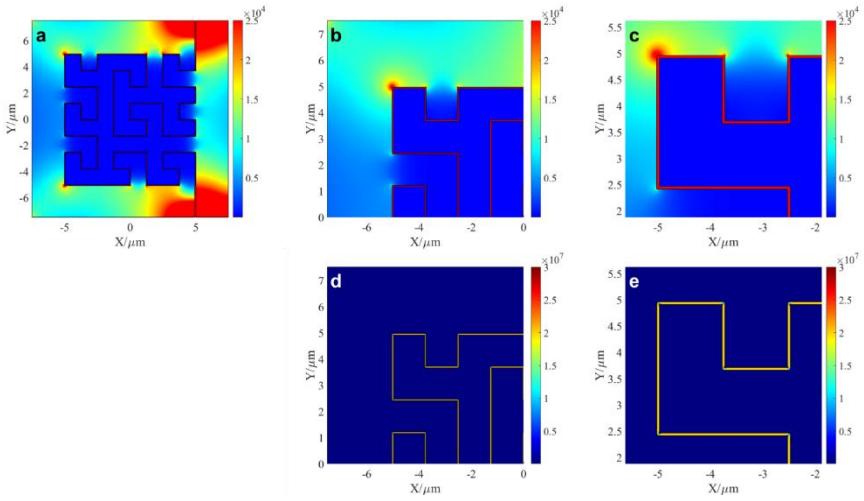

Fig. S46. COMSOL simulations of the electric field intensity distributions (unit: V/m) of the R-1 FNSC with 50 nm-interspace. (a) Electric field intensity distribution of the device. (b-c) Partial enlarged views to show the electric filed intensity distribution of the electrodes. (d-e) Partial enlarged views to show the electric filed intensity distribution of 50 nm-interspace.

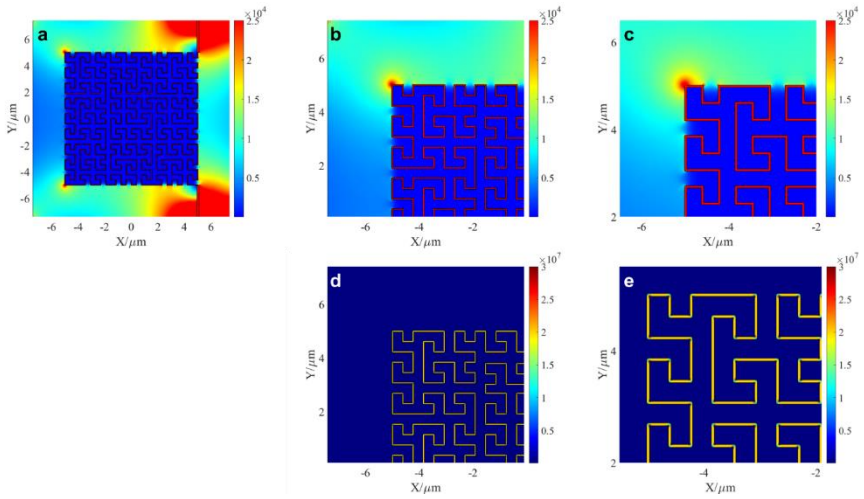

Fig. S47. COMSOL simulations of the electric field intensity distributions (unit: V/m) of the R-2 FNSC with 50 nm-interspace. (a) Electric field intensity distribution of the device. (b-c) Partial enlarged views to show the electric filed intensity distribution of the electrodes. (d-e) Partial enlarged views to show the electric filed intensity distribution of 50 nm-interspace.

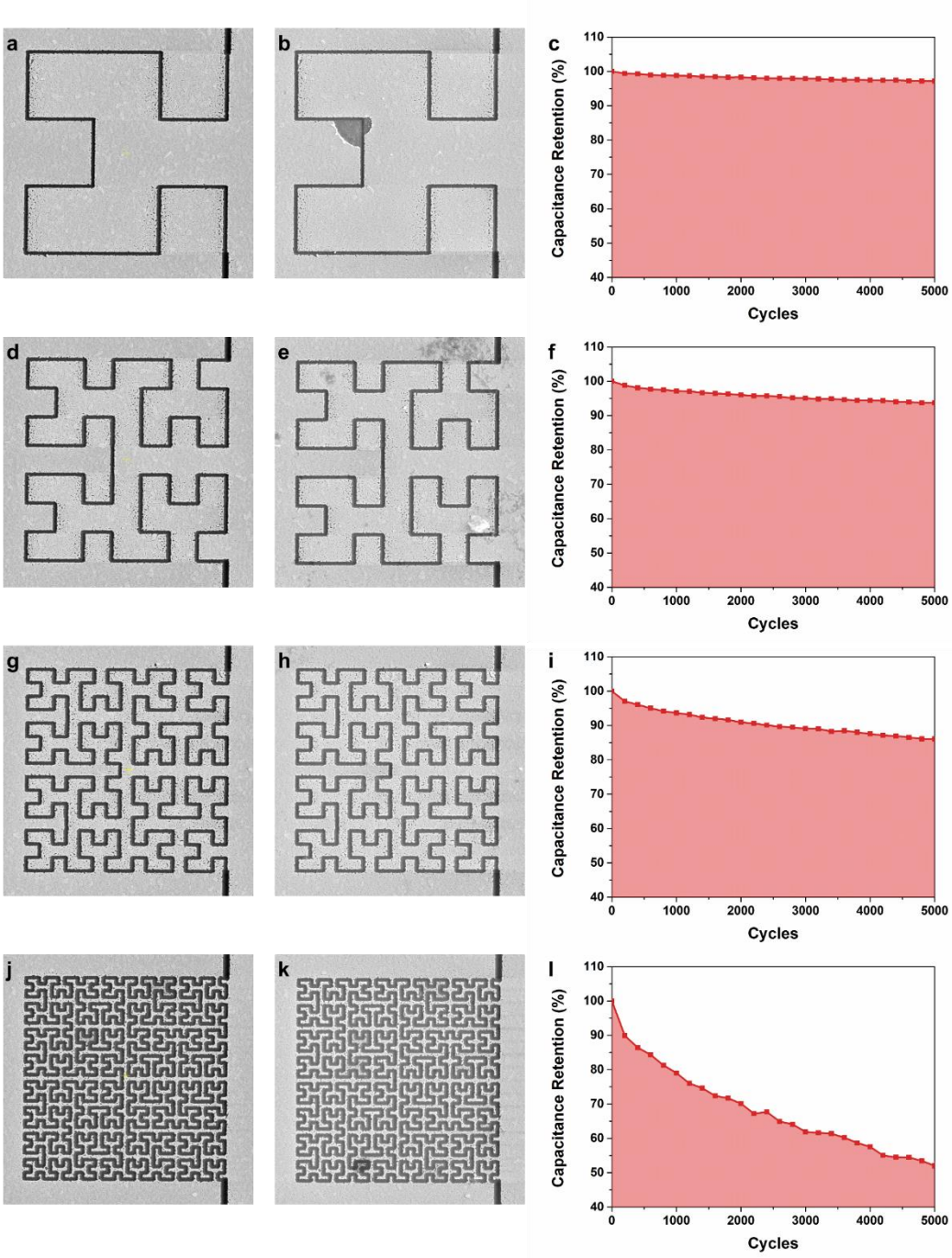

Fig. S48: Cycling stability of the FNSCs with Hilbert designs. SEM images of **H-1** (a), **H-2** (d), **H-3** (g) and **H-4** (j) FNSCs before cycling tests, respectively. SEM images of **H-1** (b), **H-2** (e), **H-3** (h) and **H-4** (k) FNSCs after 5000 charge-discharge cycles, respectively. Capacitance retention of **H-1** (c), **H-2** (f), **H-3** (i) and **H-4** (l) FNSCs, respectively.

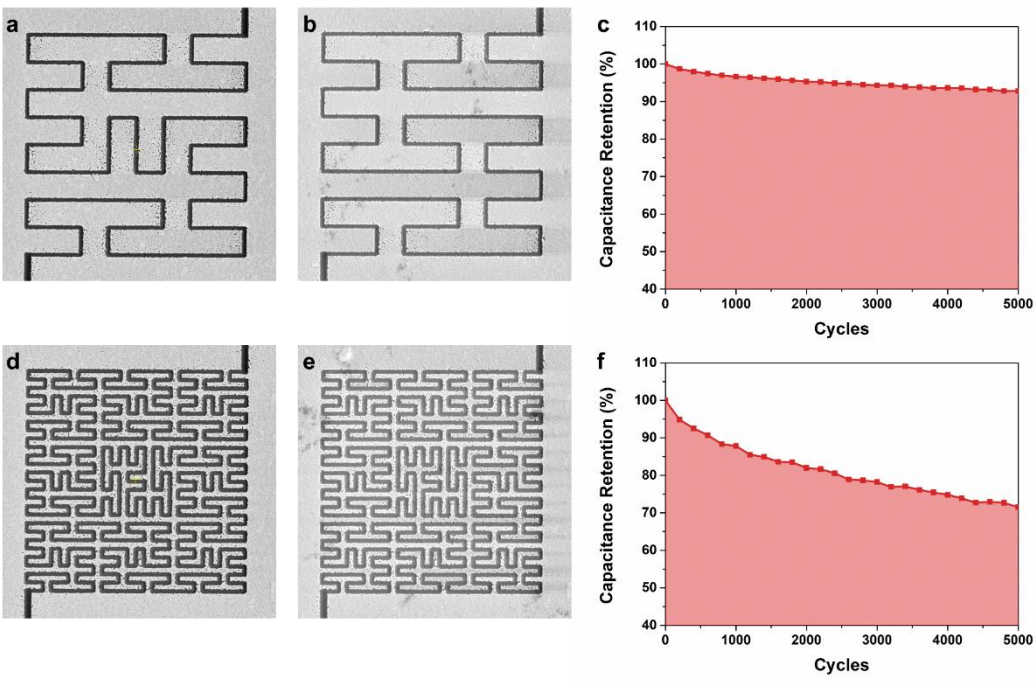

Fig. S49. Cycling stability of the FNSCs with Peano designs. SEM images of **P-1** (a) and **P-2** (d) FNSCs before cycling tests, respectively. SEM images of **P-1** (b) and **P-2** (e) FNSCs after 5000 charge-discharge cycles, respectively. Capacitance retention of **P-1** (c) and **P-2** (f) FNSCs, respectively.

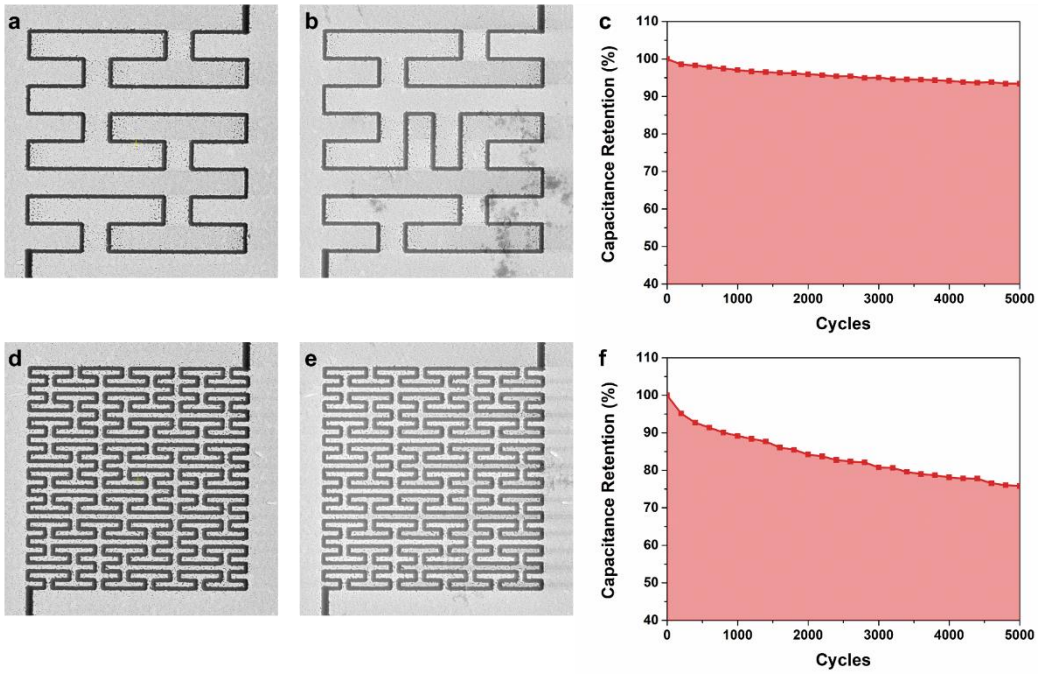

Fig. S50. Cycling stability of the FNSCs with Peano S designs. SEM images of **PS-1** (a) and **PS-2** (d) FNSCs before cycling tests, respectively. SEM images of **PS-1** (b) and **PS-2** (e) FNSCs after 5000 charge-discharge cycles, respectively. Capacitance retention of **PS-1** (c) and **PS-2** (f) FNSCs, respectively.

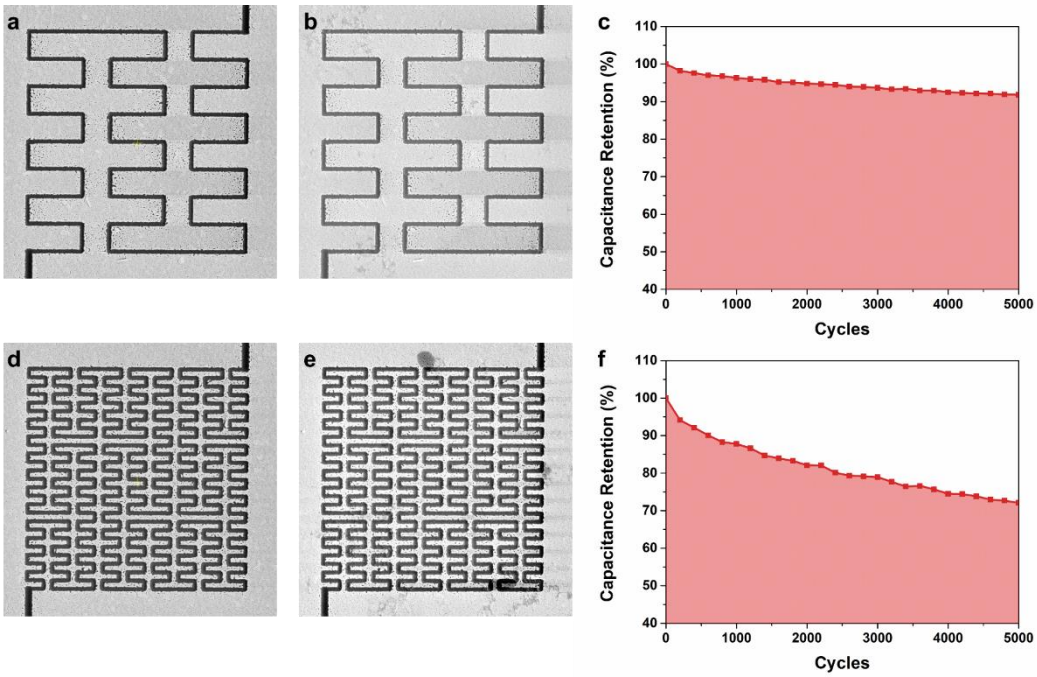

Fig. S51. Cycling stability of the FNSCs with Luxburg I designs. SEM images of **LI-1** (a) and **LI-2** (d) FNSCs before cycling tests, respectively. SEM images of **LI-1** (b) and **LI-2** (e) FNSCs after 5000 charge-discharge cycles, respectively. Capacitance retention of **LI-1** (c) and **LI-2** (f) FNSCs, respectively.

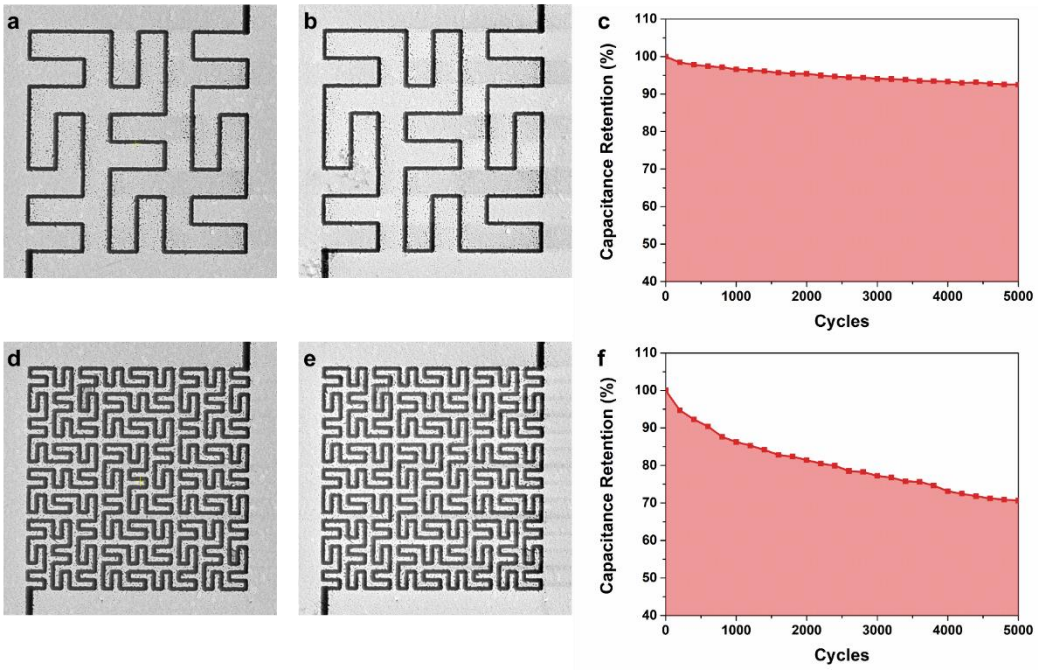

Fig. S52. Cycling stability of the FNSCs with Luxburg II designs. SEM images of **LII-1** (a) and **LII-2** (d) FNSCs before cycling tests, respectively. SEM images of **LII-1** (b) and **LII-2** (e) FNSCs after 5000 charge-discharge cycles, respectively. Capacitance retention of **LII-1** (c) and **LII-2** (f) FNSCs, respectively.

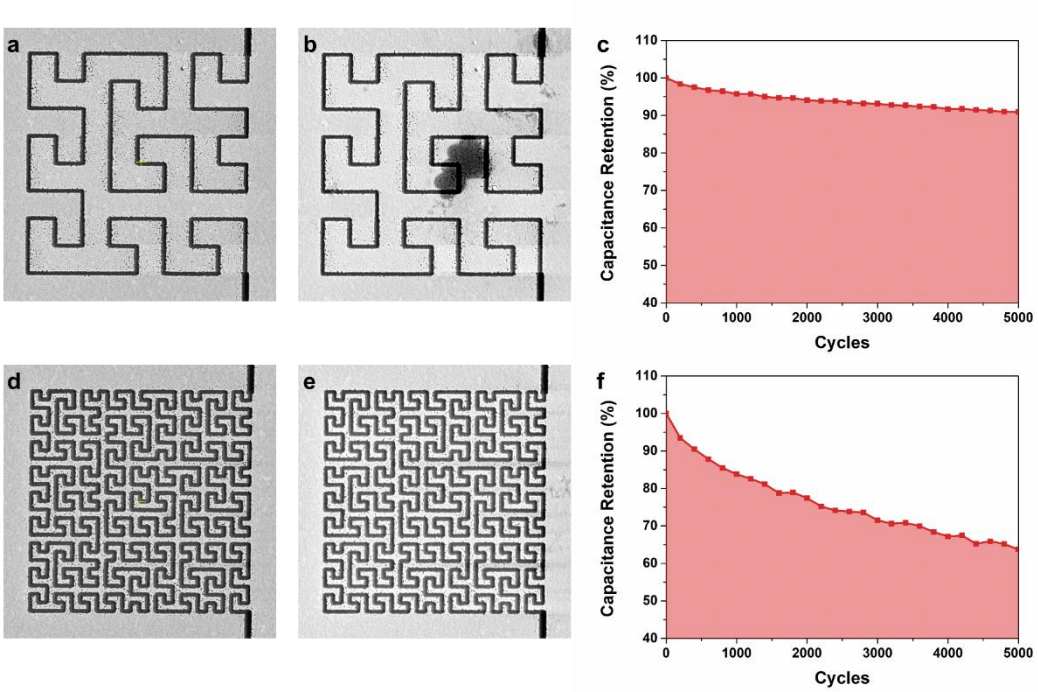

Fig. S53. Cycling stability of the FNSCs with Luxburg I designs. SEM images of **R-1** (a) and **R-2** (d) FNSCs before cycling tests, respectively. SEM images of **R-1** (b) and **R-2** (e) FNSCs after 5000 charge-discharge cycles, respectively. Capacitance retention of **R-1** (c) and **R-2** (f) FNSCs, respectively.

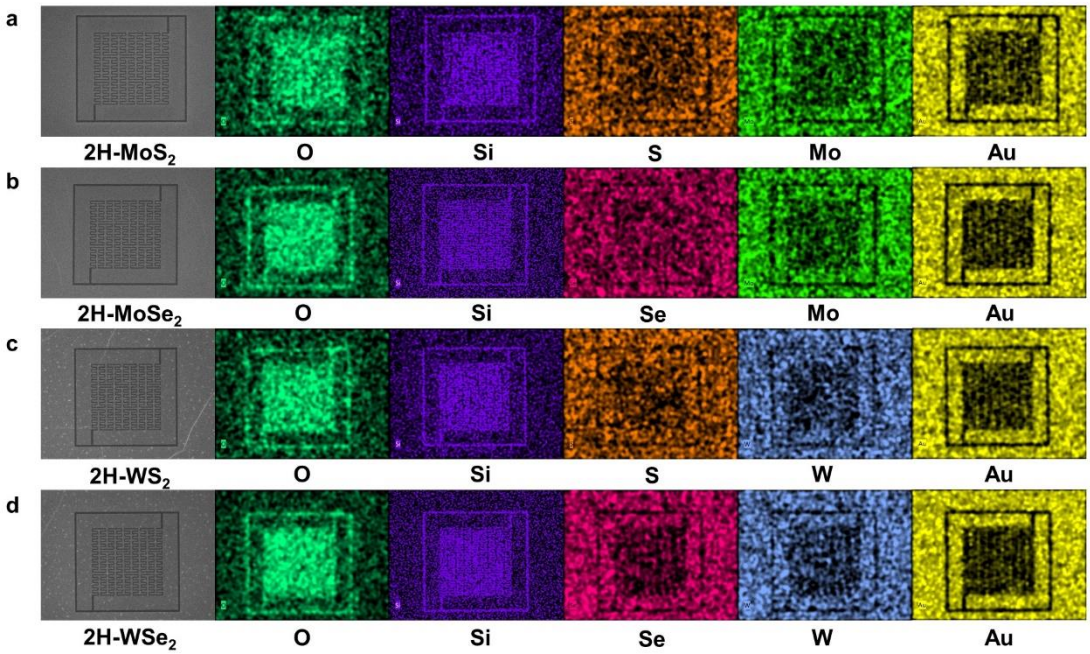

Fig. S54. SEM and EDX mapping images of LI-2 FNSCs fabricated on other TMD films. **(**a) 2H-MoS_2, (b) 2H-$MoSe_2$, (c) 2H-WS_2 and (d) 2H-WSe_2 LI-2 FNSCs. (The size of a single FNSC is 15 μm ×15 μm.)

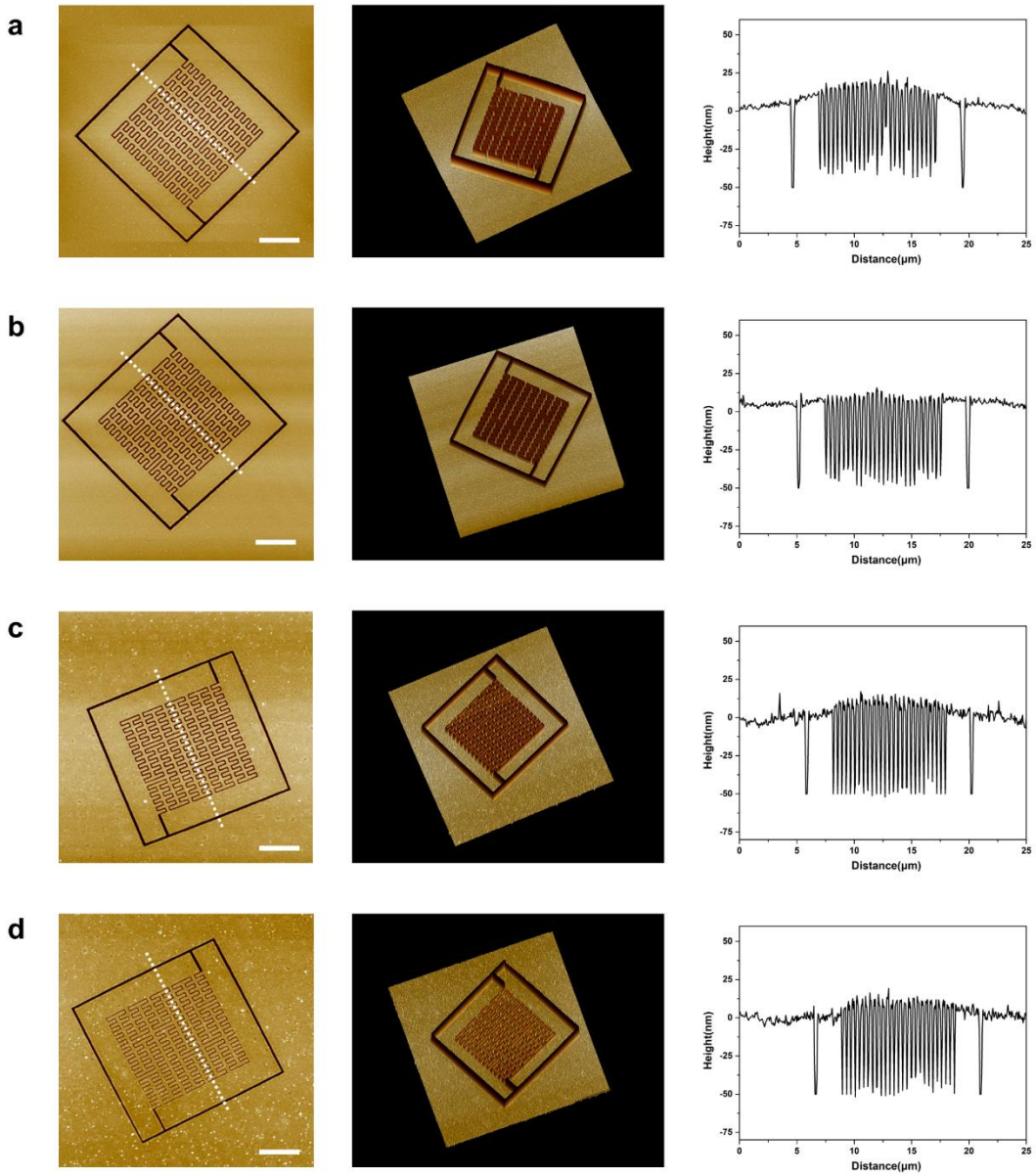

Fig. S55. 2D AFM images, bottom view 3D AFM images and AFM height profiles corresponding to the dashed lines of LI-2 FNSCs fabricated on other TMDs. (a) 2H-MoS_2, (b) 2H-$MoSe_2$, (c) 2H-WS_2 and (d) 2H-WSe_2 LI-2 FNSCs. (The scale bars are 5 μm.)

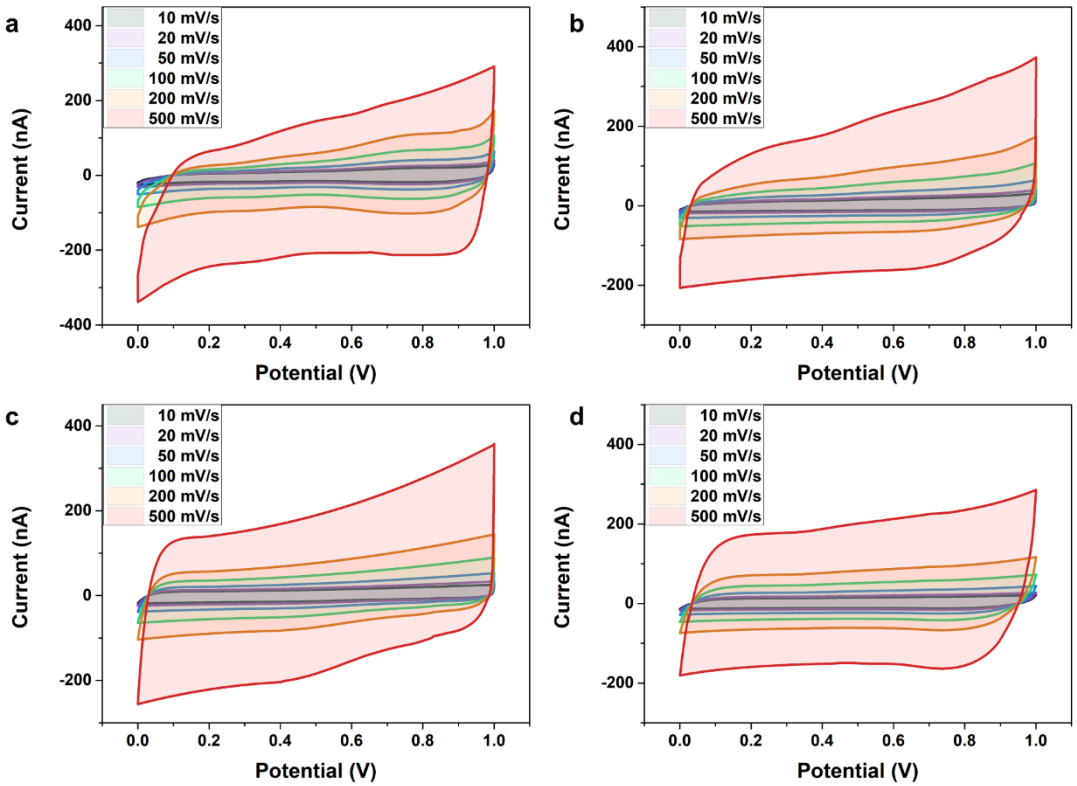

Fig. S56. CV curves of LI-2 FNSCs fabricated on other TMDs. (a) 2H-MoS_2, (b) 2H-$MoSe_2$, (c) 2H-WS_2 and (d) 2H-WSe_2 LI-2 FNSCs.

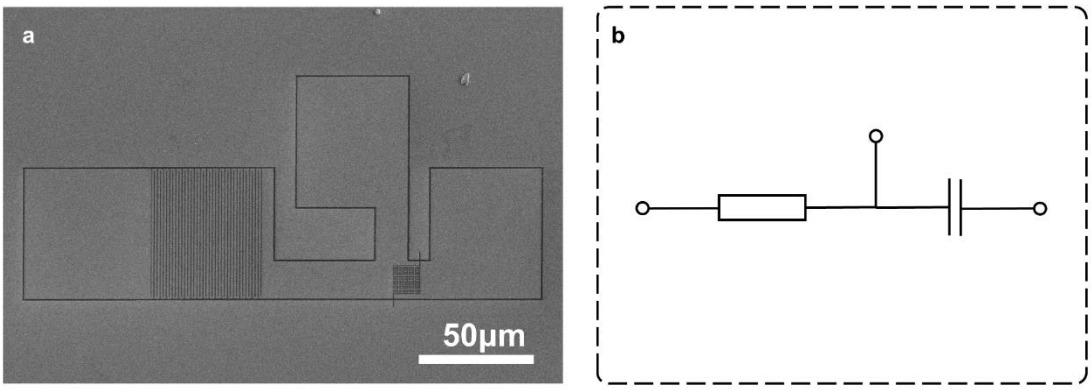

Fig. S57. (a) A micro circuit manufactured by FIB direct-writing on commercial MoS_2 film, in which a resistor is connected in series with the FNSC. (b) The corresponding circuit diagram.

Table S1. Comparison of capacitive performances of MSCs, NSCs and FNSCs.

Devices	**Materials**	**Dimension*** (μm)		**Thickness** (μm)	**Areal Capacitance** ($mF \cdot cm^{-2}$)	**Volumetric Capacitance** ($F \cdot cm^{-3}$)	**Patterning technique**	**Ref.**
		W	**I**					
MSC	SiNWs	4472	4472	6	0.0367	0.06	stacking	*Ref.23 in the text*
	MPG	210	70	0.015	0.0807	17.9	Oxygen plasma etching	*Ref.24 in the text*
	BNG	210	70	0.008	0.0976	~25.6	Oxygen plasma etching	*Ref.25 in the text*
	GF	550	200	0.4	0.441	11	Inkjet Printed	*Ref.26 in the text*
	RGO	400	400	0.025	0.462	~100	Photolithography	*Ref.27 in the text*
	GQD	230	200	0.312	0.534	17.1	Photolithography	*Ref.28 in the text*
	OLC	218	100	7	~1.0	1.3	Photolithography	*Ref.29 in the text*
	PANi	100	500	0.4	1.17	25.4	Photolithography	*Ref.30 in the text*
	MOF	150	~450	$\sim 10^{-1}$	1.36	-	Laser writing	*Ref.31 in the text*
	CF	400	400	5	1.57	3.1	Laser writing	*Ref.32 in the text*
	HACNT	300	140	~0.3	2.27	76	Oxygen plasma etching	*Ref.33 in the text*
	LSG	330	150	7.6	2.32	3.05	Laser writing	*Ref.34 in the text*
	AC	500	125	5	4.69	9.4	Screen Printing	*Ref.35 in the text*
	RGO-CNT	100	50	~5	5.5	6.1	Photolithography	*Ref.36 in the text*
	PRC	25	25	5	6.56	13.1	Photolithographic	*Ref.37 in the text*
NSC (IDE)	1T'-$MoTe_2$	0.40	0.10	0.005	9.52	18700	FIB etching	*Ref.9 in the text*
	1T'-$MoTe_2$	0.62	0.05	0.005	9.67	19340	FIB etching	This work
FNSC	**1T'-$MoTe_2$**	**0.33**	**0.05**	**0.005**	**15.1**	**30200**	**FIB etching**	**This work**
	2H-MoS_2	0.33	0.05	0.005	3.98	7960	FIB etching	This work
	2H-$MoSe_2$	0.33	0.05	0.005	2.80	5600	FIB etching	This work
	2H-WS_2	0.33	0.05	0.005	2.85	5700	FIB etching	This work
	2H-WSe_2	0.33	0.05	0.005	2.40	4800	FIB etching	This work

*W: width of microelectrode fingers, I: interspace between microelectrodes.

Table S2: Fitting parameters of $i/v^{1/2}$ *vs.* $v^{1/2}$

Interspace	50 nm	100 nm	200 nm	300 nm
k_1	1059.9	610.3	316.1	229.8
k_2	29.0	27.0	24.8	21.7

Table S3: The current contributions of the FNSCs with different interspaces

Scan rate (mV/s)		**10**	**20**	**50**	**100**	**200**	**500**
50 nm	capacitive	78.5%	83.8%	89.1%	92.0%	94.2%	96.3%
	diffusion-controlled	21.5%	16.2%	10.9%	8.0%	5.8%	3.7%
100 nm	capacitive	69.3%	76.2%	83.5%	87.7%	91.0%	94.1%
	diffusion-controlled	30.7%	23.8%	16.5%	12.3%	9.0%	5.9%
200 nm	capacitive	56.1%	64.3%	74.0%	80.1%	85.1%	90.0%
	diffusion-controlled	43.9%	35.7%	26.0%	19.9%	14.9%	10.0%
300 nm	capacitive	51.4%	59.9%	70.3%	77.0%	82.5%	88.2%
	diffusion-controlled	48.6%	40.1%	29.7%	23.0%	17.5%	11.8%

Table S4: Repeatability of the performances of the FNSCs

Areal capacitance	**IDE-1**	**IDE-2**	**IDE-3**	**IDE-4**	**H-1**	**H-2**	**H-3**	**H-4**
Samples (mF/cm^2)	5.19	6.19	9.19	5.91	5.74	8.64	9.40	3.76
	5.18	6.50	8.49	5.68	5.84	7.69	11.05	5.40
	5.16	6.25	8.67	6.33	5.92	7.84	11.51	4.63
	5.11	6.47	8.48	5.66	5.70	7.60	12.65	5.65
	5.29	6.41	8.47	5.70	5.82	8.23	11.37	4.95
	5.23	6.33	8.88	6.04	5.74	7.69	12.41	7.01
	5.23	6.48	9.67	7.79	5.89	7.68	12.16	4.70
	5.32	6.47	8.44	6.42	5.71	7.80	10.79	6.36
	5.12	6.50	8.94	7.72	5.72	8.26	10.18	3.88
	5.35	6.08	8.93	6.02	5.78	7.99	9.98	4.94
Maximum (mF/cm^2)	5.35	6.50	9.67	7.79	5.92	8.64	12.65	7.01
Average (mF/cm^2)	5.22	6.37	8.82	6.33	5.79	7.94	11.15	5.13
SD (mF/cm^2)	0.08	0.15	0.39	0.79	0.08	0.33	1.08	1.02
C.V. (mF/cm^2)	1.54%	2.36%	4.48%	12.55%	1.38%	4.22%	9.73%	19.82%

References

1. P. Zhuang, Y. Sun, P. Dong, W. Smith, Z. Sun, Y. Ge, Y. Pei, Z. Cao, P. M. Ajoyan, J. Shen and M. Ye, Adv. Funct. Mater., 2019, 29, 1901290.

2. M. Liu, Z. J. Wang, J. X. Liu, G. J. Wei, J. Du, Y. P. Li, C. H. An and J. Zhang, J. Mater. Chem. A., 2017, 5, 1035-1042.